Effect of oxidation on the optical properties of Zn_3N_2 powders

by

Helaleh Alimohammadi

B.Sc., University of Tehran, 2007

A Thesis Submitted in Partial Fulfillment

Of the Requirements for the Degree of

MASTER OF APPLIED SCIENCE

in the Department of Electrical and Computer Engineering

University of Victoria

Supervisory Committee

Effect of oxidation on the optical properties of Zn_3N_2 powders

by

Helaleh Alimohammadi

B.Sc., University of Tehran, 2007

Dr. Thomas Tiedje, Department of Electrical and Computer Engineering
Supervisor

Dr. Tao lu, Department of Electrical and Computer Engineering
Departmental Member

Abstract

Supervisory Committee
Dr. Thomas Tiedje, Department of Electrical and Computer Engineering
Supervisor
Dr. Tao lu, Department of Electrical and Computer Engineering
Departmental Member

Zinc nitride is currently attracting research interest because of its potential for novel electronic and photonic properties. In this thesis the optical properties of Zn_3N_2 powders have been investigated by photoluminescence (PL) and diffuse reflectance spectroscopy (DR) measurements. The micro structure and composition of zinc nitride were assessed by scanning electron microscopy (SEM) and powder X-ray diffraction (PXRD). Measurements of PL, PXRD and DR were carried out on zinc nitride powder samples with different oxygen-nitrogen (O/N) ratios. Photoluminescence spectroscopy of the zinc nitride powder samples allows us to find the optical bandgap of the samples. To the best of our knowledge, this is the first report on the low temperature photoluminescence of zinc nitride powder. This showed us how the band gap energy depends on temperature. The diffuse reflectance measurement let us determine a direct bandgap of 1.12eV for Zn_3N_2 powders and the PL measurements also demonstrated emission at the same photon energy. In this work, the effect of oxidation on the optical properties has been investigated. The surface oxidation of Zn_3N_2 powders and the oxygen-nitrogen (O/N) ratio were detected through PXRD scans. Our measurement show that the optical bandgap energy shifts to lower energy due to the oxygen incorporation. The reduction of the Zn_3N_2 bandgap by oxygen incorporation can be explained by a resonant interaction between the extended states of the conduction band of Zn_3N_2 and localized oxygen states near the conduction band edge. Additionally, the thermal nitriding process was carried out on the oxidized Zn_3N_2 powders to vary the O/N ratio which increased the bandgap energy. From our result, the optical bandgap of the Zn_3N_2 powders is estimated to be ~1.2 eV which decreases by small amount of oxygen contamination due to exposure to air. Powder XRD measurements of thermal oxidation of Zn_3N_2 indicated that the oxidation of these powders is slow at room temperature.

Table of Contents

Supervisory Committee ii
Abstract iii
List of tables v
List of figures vi
Acknowledgments viii
Dedication ix
1. Introduction 1
2. Theory of measurement techniques 3
X-Ray Powder Diffraction (PXRD) 3
Photoluminescence (PL) 4
Low temperature photoluminescence 5
Diffuse reflectance spectroscopy (DR) 5
Absorption of powder sample 6
Band gap energy calculation 8
Scanning electron microscopy (SEM) 8
3. Experimental Methods 9
Sample preparation 9
Scanning electron microscopy 10
Photoluminescence setup: 10
Low temperature Photoluminescence: 12
Diffuse Reflectance Spectroscopy (DRS) 14
Powder X-ray Diffraction Setup 15
Thermal Nitriding Setup 16
4. Experimental Results 17
Scanning Electron Microscopy (SEM) 17
Powder X-ray diffraction (PXRD) 19
Photoluminescence measurements 24
Absorption and bandgap measurement 30
Thermal nitriding effect on the bandgap energy 37
Thermal oxidation of zinc nitride powder 39

5. Discussion 48
Conclusion 51
References 53

List of tables

Table 1. The oxidation content is shown for different zinc nitride powders estimated by PXRD 22
Table 2**.** Optical band gaps extracted from PL spectra and other published values. The percentage of O atoms within different zinc nitride powders was estimated by PXRD. 38

List of figures

Figure 2-1. Comparison between radiative band to band recombination and non-radiative defect recombination 5
Figure 2-2. The schematic of the principle of diffuse reflectance spectroscopy 6
Figure 3-1. SEM machine (Hitachi S-4800) 10
Figure 3-2. Photoluminescence setup 12
Figure 3-3. Low temperature photoluminescence setup 13
Figure 3-4.The schematic diagram of optical diffuse reflectance spectroscopy setup 15
Figure 3-5. The schematic of the typical process in PXRD machine 16
Figure 3-6. Schematic diagram of horizontal quartz tube furnace system. 17
Figure 4-1. SEM images of the morphology of our Zn_3N_2 powders 18
Figure 4-2 (a) High magnification SEM images of selected Zn_3N_2 particles (cylindrical shape) 18
Figure 4-3. XRD pattern of Zn_3N_2 powder with the crystal indices (hkl) marked 20
Figure 4-4. (a) Perspective view of the atomic structure of bulk zinc nitride. (b) The arrangement of zinc atoms (as white spheres) around 2 different types of nitrogen atoms as blue and yellow spheres in 8b and 24d Wyckoff positions. 21
Figure 4-5. XRD patterns: (a) fresh Zn_3N_2 Powder (S1), (b) sample exposed to air for one month (S2), (c) the sample was exposed to air for one year ((o) indicates ZnO peaks) 23
Figure 4-6. Photoluminescence spectrum of Zn_3N_2 powder at RT using different excitation lasers (488nm blue laser and 532nm green laser) 24
Figure 4-7. Photoluminescence spectra of Zn_3N_2 powder at RT using a 345nm He-Cd laser 25
Figure 4-8. Temperature dependence of photoluminescence spectrum for Zn_3N_2 powder 27
Figure 4-9. Temperature dependence of the band gap energy of Zn_3N_2 powder fitted with the Bose-Einstein equation 28
Figure 4-10. The PL spectra at room temperature shows an emission peak at 1.12eV for S1and 0.95eV for S2 and 0.85eV for S3. 29
4-11. Plot (a) is reflectance spectra of samples S1, S2, and S3 and plot (b) is Kubelka-Munk transformed reflectance spectra or KM absorption coefficient of S1, S2, and S3 31
4-12. A plot of $[\boldsymbol{FR\infty h\nu}]\mathbf{2}$ as a function of photon energy for three different samples of Zn_3N_2 powder 33
4-13. UV-Vis spectroscopy of silicon results having bandgap energy of 1.04eV 34
Figure 4-14. Diffuse reflectance spectrum of silicon powder confirms the bandgap energy value around 1.04eV. 35
Figure 4-15. UV-Vis spectroscopy of sample S3 indicates the bandgap energy of 0.78 eV which is close to our DR result 36
Figure 4-16. The PL spectra of the oxidized Zn_3N_2 powder has an emission centered at 0.85eV and 1.2eV after thermal nitriding process 38

Figure 4-17. Powder X-ray diffraction patterns following thermal oxidation of Zn_3N_2 powder for 2 hours at temperatures between 200^o and 700^{o}C. 41
Figure 4-18. Powder X-ray diffraction patterns following thermal oxidation of Zn_3N_2 powders at temperatures between 400^o-700^{o}C in the 2θ range from 31^o to 38^o. 42
Figure 4-19. Triangular points and circular points show the quantity of Zn_3N_2 and ZnO at different temperature respectively. The lines are logistic curves fitted to the experimental data 44
Figure 4-20. X-ray diffraction patterns of zinc nitride powder after thermal oxidation in air at 500^{o}C for different lengths of time. 46
4-21. Expanded (321) peak of Zn_3N_2 and (002) peak of ZnO in air-annealed zinc nitride powder 47
Figure 5-1. Schematic energy diagram for the oxygen doped Zn_3N_2 which shows the conduction band interacts with narrow energy band formed by adding small amount of oxygen 49
Figure 5-2. Schematic of Zn_3N_2 particles after oxidizing and nitriding 50

Acknowledgments

I would like to take this chance to thank several individuals that this work would not have been possible without their personal and practical support.

My sincere gratitude goes to my supervisor Dr. Thomas Tiedje for giving me this opportunity to work under his supervision. I would like to thank him for his continued support for guiding me during my research. His timely advice, encouragement helped me to overcome all challenges that I faced during this work.

Beside my supervisor, my thanks go to rest of my committee member for their time, advice and interest to my research.

Also I am very grateful to be able to work with responsive and knowledgeable colleagues in Molecular Beam Epitaxy Laboratory at the University of Victoria, Peng, Vahid, Masha and Lana.
Their presence, constant help and moral support helped me considerably in this meaningful journey.

Dedication

To Haleh, my best motive

and

My family for their unconditional love and support

1. Introduction

Zinc nitride is one of the group II-V semiconductors which are much less studied materials than III-V semiconductors. For this reason, most of its electronic and photonic properties need further investigation in detail. Zinc nitride is an excellent choice for mass production in the electronic industry because of its non toxic nature and low materials cost. In order to use zinc nitride in optoelectronic devices [1], photovoltaic and sensor applications [2], we need to get accurate information about its fundamental properties such as its optical bandgap. Until now, different bandgap values between 0.85eV [3] to 3.4eV [4] have been reported. The reported values of the bandgap vary depending on the growth techniques and conditions for synthesizing Zn_3N_2, which makes its bandgap a controversial issue. Recently, the effect of oxygen on bandgap energy of Zn_3N_2 has been received special attention from researchers. However the effect of oxygen contamination on the optical properties of Zn_3N_2 is still unclear.

Zinc nitride powder was first synthesized by Juza and Hahn in 1940; it has remained a relatively unstudied material for the past 50 years [5]. Partin *et al*. [6] refined the Zn_3N_2 structure from powder diffraction data for the first time. Zinc nitride has a black color and the antibixbyite structure. Futushara et al. [7] investigated the optical properties of Zn_3N_2 thin films produced by reactive RF magnetron sputtering which had a direct bandgap of 1.23eV. Furthermore recent theoretical calculations such as density-functional theory (DFT) have shown that Zn_3N_2 is expected to have a small bandgap in the range of 0.9-1.2 eV [8, 9]. If the bandgap is in the 1.1-1.4 eV range, zinc nitride can be considered as a promising material for solar cell applications. Zinc nitride has been prepared in different nanostructures with different reported bandgap values, including nanoneedles (E_g=2.7 eV) [10], hollow structures (E_g=2.8 eV) [11], and zinc nitride nanocrystals (E_g=1eV) [12]. Also, thin films of Zn_3N_2 have been produced by a variety of the

methods including pulsed laser deposition [13], metal organic vapour deposition [14], and molecular beam epitaxy [15]. Lately, single crystal Zn_3N_2 films have been grown by plasma-assisted molecular beam epitaxy with an optical bandgap around 1.25–1.28 eV [16]. Therefore after multiple studies, the exact bandgap value of Zn_3N_2 is still a subject of debate since many different bandgap values have been reported.

In this study, some optical and micro-structure properties of the zinc nitride powder have been investigated. The scanning electron microscopy (SEM) and powder x-ray diffraction (PXRD) methods were used to find the structural properties and chemical composition of Zn_3N_2 powders. Information about shape, size, and surface composition could be obtained from these methods as well as information about the presence of oxygen impurities. The optical bandgap of Zn_3N_2 has been determined through different methods. To the best of our knowledge, no report about low temperature photoluminescence of Zn_3N_2 powder has been published. In this work, the bandgap of zinc nitride powder was found using photoluminescence measurements (PL) at both low temperature and room temperature. Also the diffuse reflectance (DR) measurements were used as an additional method to obtain the optical band gap value. In addition, some UV-Vis spectroscopy measurements have been done on Zn_3N_2 powder to support our DR results. PL, DR and PXRD measurements were used to investigate the bandgap and structure of Zn_3N_2 as a function of the oxygen-nitrogen ratio. To explore the effect of oxygen contamination on the bandgap of zinc nitride, thermal nitriding experiment was utilized to change the O/N ratio within Zn_3N_2 structure. Finally, in order to explore the oxidation stability of Zn_3N_2 powder on exposure to air, thermal oxidation has been studied.

2. Theory of measurement techniques

X-Ray Powder Diffraction (PXRD)

X-ray powder diffraction is a widely used method for determining the composition of unknown polycrystalline materials. When the surface of a crystalline powder is exposed to an X-ray beam, the scattered X-ray beam produces a diffraction pattern which is characteristic of the structure. In powder X-ray diffraction, the diffraction pattern of the powder gives the information about the atomic arrangement in the crystalline solid and the value of the lattice parameter. All crystalline materials have particular diffraction patterns. So we can use the International Center for Diffraction Data (ICDD) database of diffraction patterns to identify any unknown compound. In addition, the purity of the sample can be estimated from the diffraction pattern if there is any crystalline impurity in the material.

$$n\lambda = 2\, d_{hkl} \sin\theta \tag{2-1}$$

Eq.2-1 is the Bragg's condition required for diffraction. The diffraction pattern has a peak when constructive interference occurs due to reflection from different layers. Diffraction patterns are plotted as an absolute intensity vs. the 2θ angle of the detector. To analyze powder XRD data, we need to know the relation between the Miller indices and diffraction peaks. Therefore, we first determine which Miller indices (hkl) cause diffraction peaks for the crystal structure. The space between parallel planes of atom is defined as d_{hkl} which can be found by using the observed peak position within Bragg's condition , where θ is the angle of incidence of X-rays, n is an integer and λ is the wavelength. [17]

Photoluminescence (PL)

Photoluminescence (PL) in semiconductors is a promising way to get important information on the optical bandgap and electronic property of the material. Photoluminescence occurs when an optical source excites the surface of a material with a monochromatic light beam with a photon energy higher than the bandgap energy. Then electrons absorb the photon energy and move from the valence band to the conduction band and leave behind electron-hole pairs in the conduction and valence bands. The density of excited carriers differs according to the intensity of incident photons. The excited carriers release their stored energy by transferring from the conduction band to the valance band through recombination. This recombination can be radiative by emitting photon energy or non-radiative by defect or surface recombination. The radiation caused by recombination is called photoluminescence. If we have a pure material, band to band luminescence will occur through recombination of an electron in the CB with a hole in the VB. This radiative transition can give valuable information about the band structure. If there are impurity levels inside the forbidden band gap, electrons and/or holes can get trapped by these impurities. The recombination that happens through defect levels gives rise to low energy luminescence emission or non-radiative recombination without photon emission. Sometimes, the concentration of impurities is large enough and the energy is close to the band edge. In this case the impurities can alter the bandgap. All vacancies, interstitials or substitutional impurities may cause deep level defects in semiconductors [18] [19]. On the other hand, it's not easy to ascribe the observed PL spectra peak to specific impurities or defects. Figure 2.1 shows the difference between radiative band to band recombination and defect non-radiative recombination.

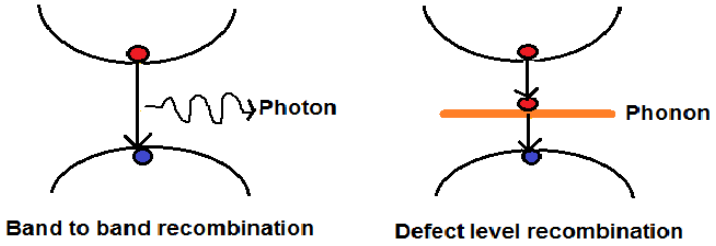

Figure 2-1. Comparison between radiative band to band recombination and non-radiative defect recombination

A PL spectrum plots the emission intensity vs. wavelength. To change the intensity as a function of wavelength to intensity as a function of energy, we can use the basic equation of photon energy which is $E = h\nu$ to find the following equation:

$$I_E(E) = I_\lambda(\frac{hc}{E})\frac{hc}{E^2} \quad (2\text{-}2)$$

where $I_E(E)$ is final PL spectrum as intensity per unit energy. In this study, we measured the PL spectrum of zinc nitride to get information about its bandgap and electronic properties which has not been investigated before in powder samples.

Low temperature photoluminescence

One of the standard ways to analyze the impurities is PL measurements at low temperature because PL measured at low temperature has sharp and strong spectral lines. This is particularly important in the case of band edge PL, in order to separate the band to band PL from the PL associated with shallow impurities [17].

Diffuse reflectance spectroscopy (DR)

Diffuse reflectance spectroscopy (DR) is a well-known technique in the analysis of the optical properties of powdered samples. When the light beam goes into powder sample, it can be reflected off the surface of a particle or transmitted through a particle, or absorbed. In powder samples, diffuse reflection means reflecting the incident light at many angles rather than at just

one angle as in the case of specular reflection. The material is assumed to be uniform, isotropic, non-fluorescent and non-glossy to be able to scatter the light [20]. Also, the scattering and absorption of light in the material change depending on the color of the material. Figure 2.2 shows the principle of near infrared (NIR) diffuse reflectance spectroscopy. The diffuse reflectance of a powder is highly dependent on the absorption coefficient and is low for strongly absorbing materials.

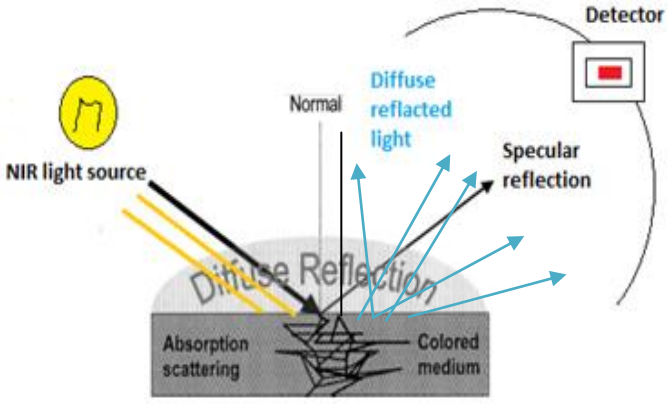

Figure 2-2. The schematic of the principle of diffuse reflectance spectroscopy

Absorption of powder sample

There are several theories for calculating the optical properties of a material, from DRS data. The simplest practical method was defined by Kubelka and Munk in 1931. According to KM theory, the most straightforward measurement that provides the information about the absorption coefficient of a powder is diffuse reflectance spectroscopy. [21]

Kubelka and Munk assumed that the light can travel only upward and downward through the layer. The symbols *I (x)* and *J (x)* represent the downward and upward flux of light, respectively which can change as they propagate through a layer of thickness dx of material by absorption and scattering processes [22][23]. Then we can write a differential equation for both fluxes as follows:

$$dI/dx = -(k+s)I + sJ \tag{2-3}$$

$$dJ/dx = (k+s)J - sI \tag{2-4}$$

The quantities s and k, in units of cm^{-1}, are called the Kubelka-Munk scattering and absorption coefficients. By defining $a=(s+k)/s$, we can rewrite the equations more simply:

$$dI/sdx = -aI + J \tag{2-5}$$

$$dJ/sdx = aJ - I \tag{2-6}$$

Reflectance from the sample is similar to the transmittance in the Beer-Lambert law and is defined by the following equation:

$$R(x) = J(x)/I(x) \tag{2-7}$$

by combining equations of 2-5, 2-6 and 2-7, we can get a single differential equation:

$$dR/(R^2 - 2aR + 1) = sdx \tag{2-8}$$

after integration by using $x=0$ and $x=x$ limits, we get

$$sx = [\{1/(p-q)\} ln \{(R-p)/(R-q)\}] \tag{2-9}$$

where p and q are roots of the equation $R^2 - 2aR + 1=0$ $\{p = a + \sqrt{a^2-1}\,, q = a - \sqrt{a^2-1}\,\}$. R_∞ is defined as the reflectance of an infinitely thick layer of the sample which means no light goes through this layer. R_∞ approaches q when $x \to \infty$. This leads us to the Kabulka-Munk equation $F(R_\infty)$ for the absorption. Solving for k/s in terms of R_∞ we find:

$$sR_\infty = [k + s - \sqrt{k(k+2ks)}] \tag{2-10}$$

$$F(R_\infty) = (1-R_\infty)^2/2R_\infty = k/s \tag{2-11}$$

By using Eq. 2-11, we can determine the ratio of k/s from one measurement of reflectance R_∞ and more information is required to get the values of k and s separately. To get R_∞ in DR measurement, we need to use the following formula: [24]

$$R_\infty(\lambda) = R_{sample}(\lambda)/R_{Reference}(\lambda) \tag{2-12}$$

where $R_{Reference}$ is a white reflectance standard.

Band gap energy calculation

Now we have a relation between absorption coefficient and diffuse reflectance. Next step is to find a relation between diffuse reflectance and bandgap energy. There is a famous equation in the case of a parabolic band structure for a direct bandgap semiconductor that relates the absorption coefficient to the band gap energy E_g [25]:

$$(\alpha h\nu)^2 = C1\left(h\nu - E_g\right) \tag{2-13}$$

where α is the linear absorption coefficient of the material, $h\nu$ is the photon energy, E_g is the bandgap and *C1* is a constant. The scattering coefficient is considered to be constant in the KM equation and this is a good assumption as refractive index also is constant in this particular area. So now we can exchange α with the ratio of $F(R_\infty)$ to conclude this equation:

$$[F(R_\infty)h\nu]^2 = C2\left(h\nu - E_g\right) \tag{2-14}$$

and then by plotting $[F(R_\infty)h\nu]^2$ versus $h\nu$, we can easily determine the value of the band gap energy E_g.

Scanning electron microscopy (SEM)

Scanning electron microscopy (SEM) is a technique for high-resolution imaging of the surface of a material. Using electrons for imaging is the principle behind a SEM machine while visible light is used in a light microscope. In a SEM system, a thermal or field emission source produces the beam of incident electrons above the sample chamber by heating a tungsten filament, or by a field emission cathode in vacuum. The energy of the incident electrons can be varied depending on the accelerating voltage. The electrons are directed on the surface of sample as a small beam by using electromagnetic lenses and scanning coils near the end of the column. When incident electrons penetrate a sample, secondary electrons are generated near the sample surface by

inelastic scattering. The emitted secondary electrons from an extremely small area are sensitive to specific information about topographic features of the sample surface. Therefore, SEM high resolution images are created by using the secondary electron signals which are detected by an electron detector. [44]

3. Experimental Methods

In this chapter, a description of all techniques and equipment that have been used in different experiments are provided.

Sample preparation

Zn_3N_2 powders have been used for measurements in the PL, Powder XRD, and SEM setups. To do low temperature PL and DR measurements, all samples were in the form of a pressed pellet of powder formed with a pellet-forming die. Cylindrical pellets have 1cm diameter and about 0.5mm thick which made by applying a force of approximately 4 tons.

Zinc nitride powder with a purity of 99% was purchased from Alfa Aesar. According to G. Harris (personal communication, July11, 2016), this powder was synthesized by a nitridation reaction of Zn powder with NH_3 gas (flow rate 500 ml/min) at the nitridation temperature of 600 °C for 120 min. After this reaction solid zinc nitride was crushed to form a powder. The chemical reaction of the fabrication process is as follows:

$$4Zn(s)+6NH_3(g)\longrightarrow 2Zn_2N_3(s)+9H_2(g) \quad (3\text{-}1)$$

Measurements of PL, PXRD and DR were carried out on different zinc nitride powder samples at room temperature. There are four Zn_3N_2 powder samples (S1, S2, S3, and S4) with different oxygen contamination. S1 represents Zn_3N_2 powder after one week exposure to air. S2 and S3

powders were exposed to air for one month and one year, respectively. S4 corresponds to the partially oxidized Zn_3N_2 that was thermally nitrided.

Scanning electron microscopy

SEM is used specifically to observe sample surface, shape and size at high magnification. We used the advanced microscopy facility of the University of Victoria (Hitachi S-4800) to record SEM images. We adjusted the SEM operation with an accelerating voltage of 1 kV to have resolution as small as 5μm. Figure 3.1 shows the SEM (Hitachi S-4800). This system is equipped with two secondary electron detectors, a ring-type Yttrium Aluminum Garnet (YAG) backscattering detector and a Bruker Quantax EDX system for energy-dispersive x-ray spectroscopy (EDX).

Figure 3-1. SEM machine (Hitachi S-4800)

Photoluminescence setup:

Photoluminescence (PL) in semiconductors gives valuable information about the electronic properties of materials, such as the optical bandgap energy and the efficiency with which the material emits light. Photoluminescence occurs when an excited electron in the conduction band recombines radiatively with a hole in the valence band. In this study, we did a large number of PL measurements at both room temperature and at low temperature. The room temperature setup

is shown in figure 3.2. The sample was excited by two different lasers as our excitation source. First one was a 532 nm green laser which produces 20ns pulses from a diode-pumped frequency doubled Nd:YLF laser. The photon energy is larger than the band gap energy of the samples. The average power of the laser was 1.5 mW, at a repetition rate of 2 kHz with a peak power density of 10^4 W/cm^2. In another room temperature measurement, a 488 nm CW Ar-ion laser beam chopped at 2 kHz was used as an excitation source which had higher energy than the green laser. According to this optical setup, the emission light from the sample is collected by the first lens which is placed so that its focal point is on the illuminated spot. The second lens with the same f number as the first one, focused collimated emission light on the tip of the optical fiber. The optical fiber transferred the PL emission to a spectrograph from Acton Research (SpectraPro 3000) and then was detected by an InGaAs array detector from Roper Scientific (Model 7410-0003) which is cooled with liquid nitrogen. One of the most important factors in the PL measurements is using an optical filter to eliminate the second and higher order harmonics and laser stray light which can affect the measured PL intensity. To achieve this objective an 830nm cut off filter was placed after the lenses and before the optical fiber. Furthermore, for maximum signal collection, the NA (Numerical Aperture) of the fiber and the system of lenses has to be matched. The light-gathering ability of a lens totally depends on its f number which is defined by: $f = 1 / 2NA$. In addition, as a final correction of the PL spectra from the spectrometer, we measured the background signal in the dark and subtracted it from the PL spectrum. Also, we used p-doped GaAs a strong luminescent emitter whose bandgap is known as a reference sample to calibrate the optical setups. Additionally for PL measurement, a 345nm polarized He-Cd laser with 45 mW power was used. The laser stray light has been removed by using 550nm high pass

filter and a NIR PMT detector was utilized to detect the emission light in the range of 700-1400nm.

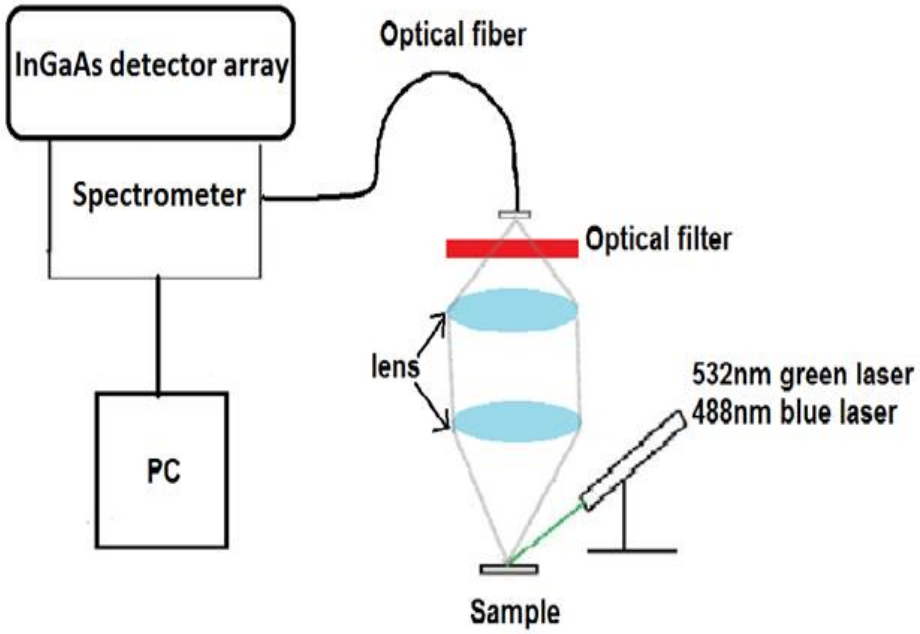

Figure 3-2. Photoluminescence setup

Low temperature Photoluminescence:

Low temp PL measurements can be considered as a proper way to make a distinction between bandgap energy and defects. For the low temperature setup, we used an optical helium cooled cryostat (CS202AI-DMX-1SS) from Advanced Research Systems Inc with three quartz optical windows. The sample is placed on copper holder which can be cooled to different temperatures as low as 4K by using a closed cycle helium gas refrigerator. The schematic diagram of this setup is shown in figure 3.3. We used a vacuum pump and a turbo pump connected to a pumping line to evacuate the inside of the cryostat. To stabilize the temperature of the sample at different values, a heater is connected to the sample holder. This heater can control the cryostat temperature in the range from 10 K to 300 K.

In our laser setup, a 488 nm Ar-ion laser beam is chopped at 2 kHz and focused on the sample surface. This was the excitation source for photoluminescence spectroscopy. We mounted our sample on the copper pillar oriented so that there was 45 degrees between the excitation beam and the emission beam. We directed the laser beam on the surface of the sample through one of the optical windows on the cryostat system with a focusing lens. We collected the emission light from the sample through the other window with another lens. The long pass 527nm filter from Thorlabs is placed before optical fiber to avoid any of the blue laser excitation from reaching the detector. Lenses focused the radiation beam on the tip of an optical fiber which is connected to the spectrograph. After that, the transferred beam was detected by the InGaAs array detector which is cooled by liquid nitrogen.

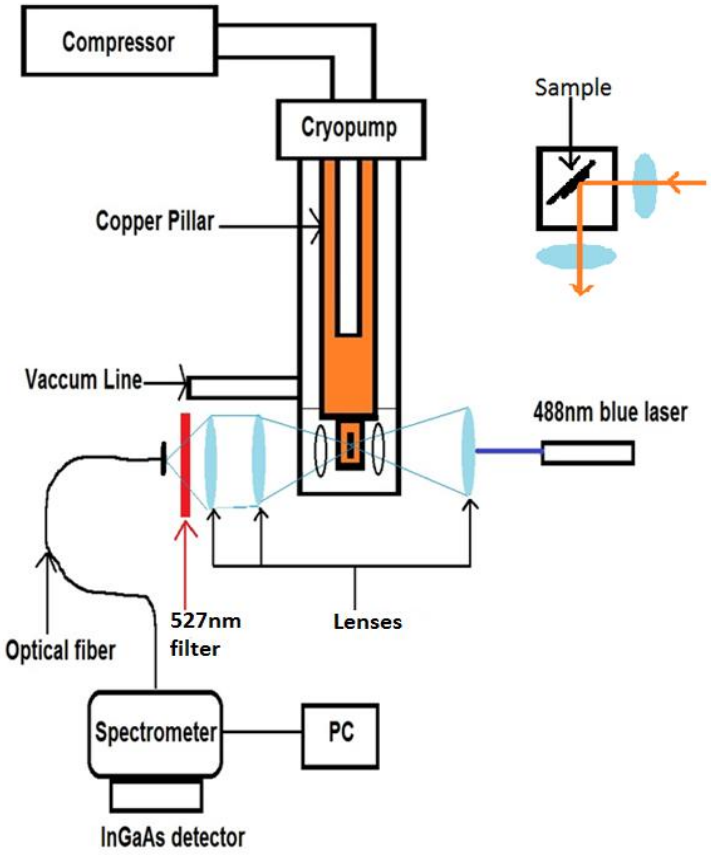

Figure 3-3. Low temperature photoluminescence setup

Diffuse Reflectance Spectroscopy (DRS)

Diffuse reflectance spectroscopy is a classical optical method for measuring the absorption of powders. We built the optical setup shown schematically in figure 3.4 to obtain our samples reflectivity. A halogen lamp was used as a light source. The light beam was directed into the entrance slit of the monochromator (ARIES FF259 spectrograph) with a focusing lens. Light travelling from the lens was chopped with an optical chopper. The output beam of the monochromator was a single wavelength beam, which was filtered and then focused on the surface of the sample by another focusing lens. In our optical setup, the angle between the excitation beam and reflected beam was 60^{o} to avoid any specular reflection.

The focusing lenses collected and collimated the reflected beam from our sample and centred it on the InGaAs detector (Model 2033). Also, a black barrier was used to block any stray light on the detector. We connected a lock-in amplifier to the detector to measure the output beam with minimal background noise. For correction of our spectra, the transfer function of our optical setup has been found and then our reflectance spectrum divided by that function to get a final reflectance spectrum. By doing this experiment in our optical setup, we can obtain $R_{\infty}(\lambda)$ which was mentioned in the previous theory section. It is bounded between 0 and 1. We used spectralon as our reference in determining the transfer function with more than 95% reflectivity in the range of (250-2500nm) for diffuse reflectance measurements.

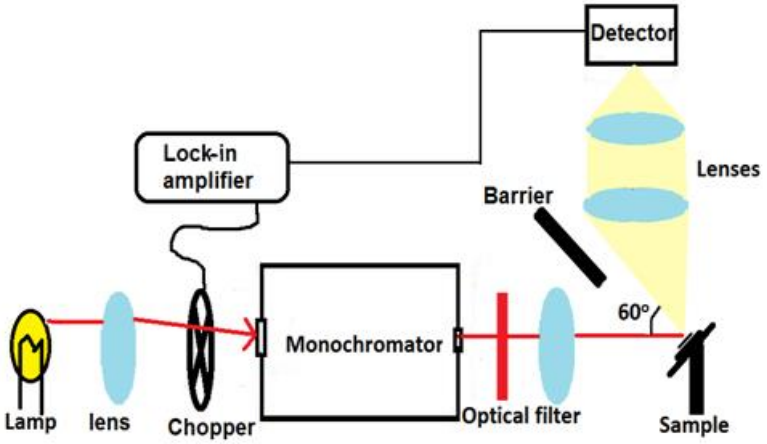

Figure 3-4.The schematic diagram of optical diffuse reflectance spectroscopy setup

Powder X-ray Diffraction Setup

A powder X-ray diffractometer consists of three basic parts: an X-ray tube, a sample stage, and a detector as shown in figure 3.5. The X-ray beam is focused on the sample at some angle θ, while the detector opposite the source reads the intensity of the diffracted X-ray, an angle 2θ away from the source path. First, in a cathode ray tube, X-rays are produced by heating a filament and then accelerating the electrons toward a Cu target. These X-rays are collimated and directed onto the sample. The intensity of the reflected X-rays is measured while slowly rotating the sample and detector. An intensity peak is observed when constructive interference occurs by satisfying the Bragg equation. A detector records and processes this X-ray signal and converts the signal into a PXRD spectrum. Phase purity was assessed from powder X-ray diffraction (PXD) data collected on a PANalytical Empyrean X-ray diffractometer with copper x-ray source. The experimental powder pattern is identified by searching against reference patterns in the database containing the patterns of > 700,000 pure compounds which was produced at the International Centre for Diffraction Data by the Joint Committee on Powder Diffraction Standards (JCPDS).[24]

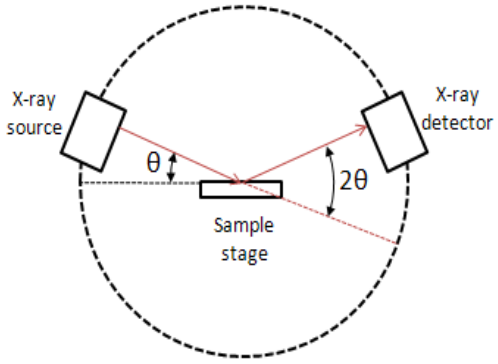

Figure 3-5. The schematic of the typical process in PXRD machine

Thermal Nitriding Setup

The thermal nitriding method was applied to study how changing the oxygen-nitrogen (O/N) ratio might influence the bandgap energy of zinc nitride powder. For the thermal nitriding process, a tube furnace with temperature programming to 1200^{o} C was used. Figure 3.6 shows the schematic diagram of a horizontal tube furnace. The sample was placed in a crucible boat that was inserted into the center of a quartz tube inside a furnace. The quartz tube was degassed and then purged with argon. The temperature of the furnace was raised up to 500^{o} C at a rate 20~25^{o} C/min under constant flow of Ar. When the tube reached the reaction temperature, ammonia NH_3 gas was passed into the quartz tube at a flow rate of 500 ml/min for 120 min. After the reaction, the furnace was cooled back down to room temperature.

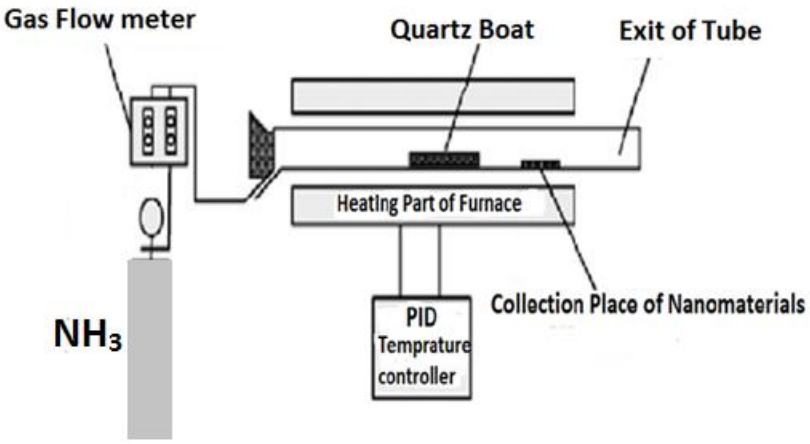

Figure 3-6. Schematic diagram of horizontal quartz tube furnace system.

4. Experimental Results

Scanning Electron Microscopy (SEM)

A micrograph of the surface morphology of Zn_3N_2 powder is illustrated in figure 4.1. As we can see, the Zn_3N_2 powder consists mainly of faceted crystals in the 1-10 μm size range. Also other irregular shapes, such as flakes, and different type of spherical particles can be observed.

Another picture with higher magnification than the first image is shown figure 4.2 (a, b). Figure 4.2 (b) clearly presents a hexagonal structure of Zn_3N_2 with a diameter of about 3-5 μm. In addition, there is another image (figure 4.2 (a)) at a different location which shows faceted particles about 7 μm in diameter. The faceted shapes suggest that the particles are single crystals.

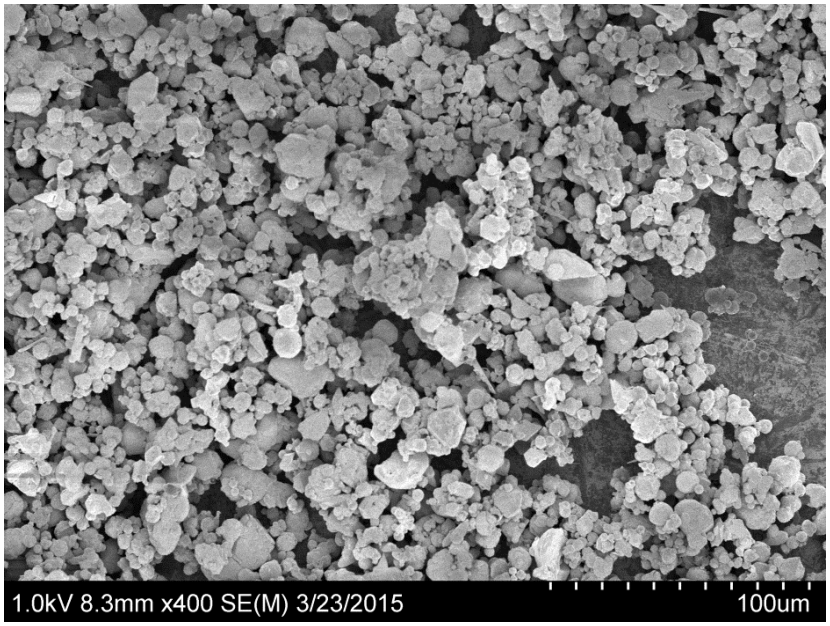

Figure 4-1. SEM images of the morphology of our Zn_3N_2 powders

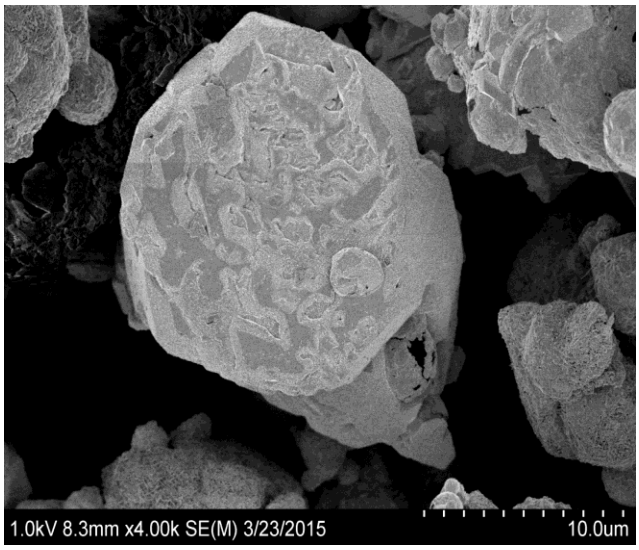

Figure 4-2 (a) High magnification SEM images of selected Zn_3N_2 particles (cylindrical shape)

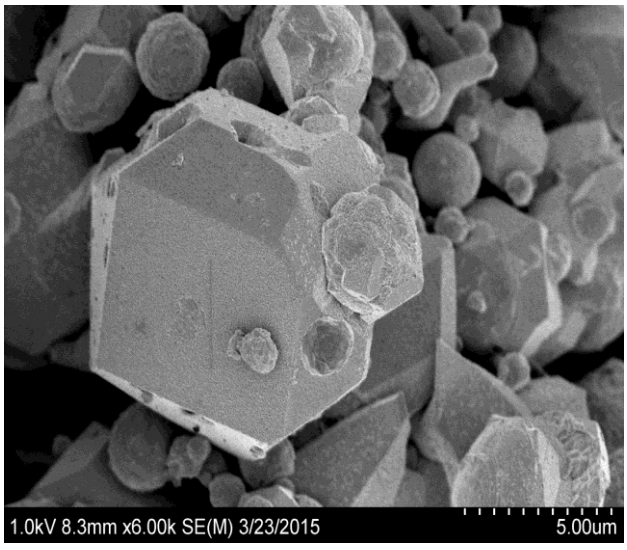

Figure 4-2 (b). High magnification SEM images of selected Zn_3N_2 particles (hexagonal shape)

Powder X-ray diffraction (PXRD)

Powder X-ray diffraction measurements were carried out on Zn_3N_2 powders to indicate the presence of crystalline impurity phases. The collected powder XRD data were cross- referenced to powder patterns generated by the International Center for Diffraction Data. An XRD scan is shown in figure 4.3 which consists of all the main peaks of Zn_3N_2 powder due to peak matching with reference data (ICDD: 04-015-6959). PXRD scan indicates that we have the main peaks of Zn_3N_2 powder. The crystal indices (h k l) are marked which match the zinc nitride powder data. Also, the lattice constant of zinc nitride powder can be calculated from Eq.4.1:

$$d = a/\sqrt{h^2 + k^2 + l^2} \tag{4.1}$$

where d is the spacing between atom layers which can be determined from Bragg's law and a is the lattice constant. The lattice constant of zinc nitride is found to be a=0.9779 nm which is in good agreement with the published value of 0.977 nm in the ICDD document.

According to the "*Principle of Crystallography*," for a body centered cubic crystal system, the reflection condition of the (*h, k, l*) peak is $h+k+l=2n$. From figure 4.3 apparently all the *hkl* indices of each peak satisfy this reflection condition. From the peaks in the XRD pattern, we conclude that zinc nitride powder has an anti-bixbyite structure. This structure is similar to CaF_2, where N atoms occupy the Ca positions and Zn atoms are located at three-fourths of the F positions [6]. Also there is a group who reported a description of the electronic structure of Zn_3N_2 by using density-functional method (DFT) shown in figure 4.4(a). As shown in figure 4.4 (b), the N atoms are placed in two separate sites represented by the 8b (1/4, 1/4, 1/4) and 24d (x, 0, 1/4) Wyckoff positions and surrounded by 6 Zn atoms nearest neighbors [9].

According to these results, the commercial powder which was prepared by reaction between Zn and ammonia NH_3 is pure zinc nitride as there are no extraneous diffraction peaks in the powder pattern. Most of the main peaks of Zn_3N_2 were marked in the powder pattern in figure 4.3.

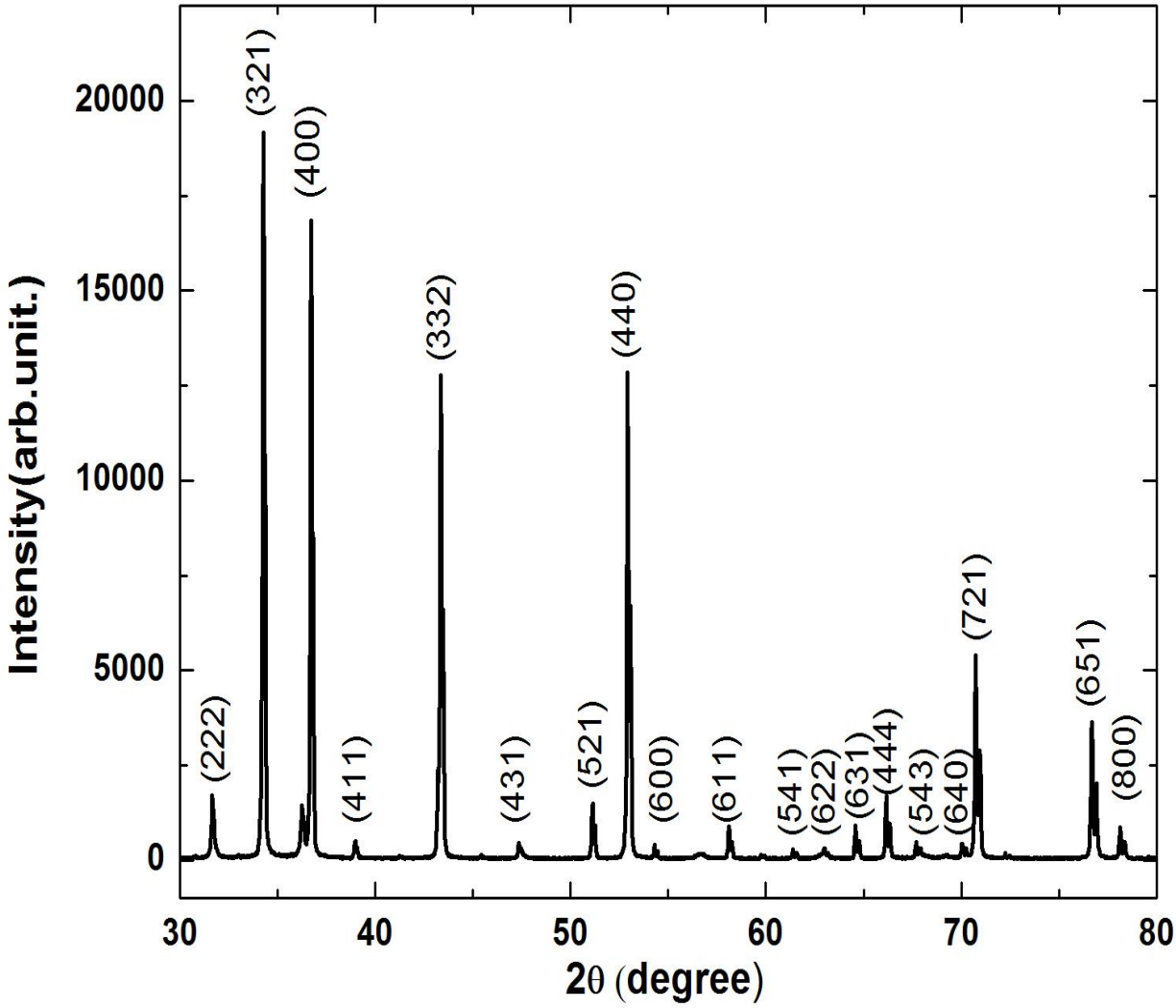

Figure 4-3. XRD pattern of Zn_3N_2 powder with the crystal indices (hkl) marked

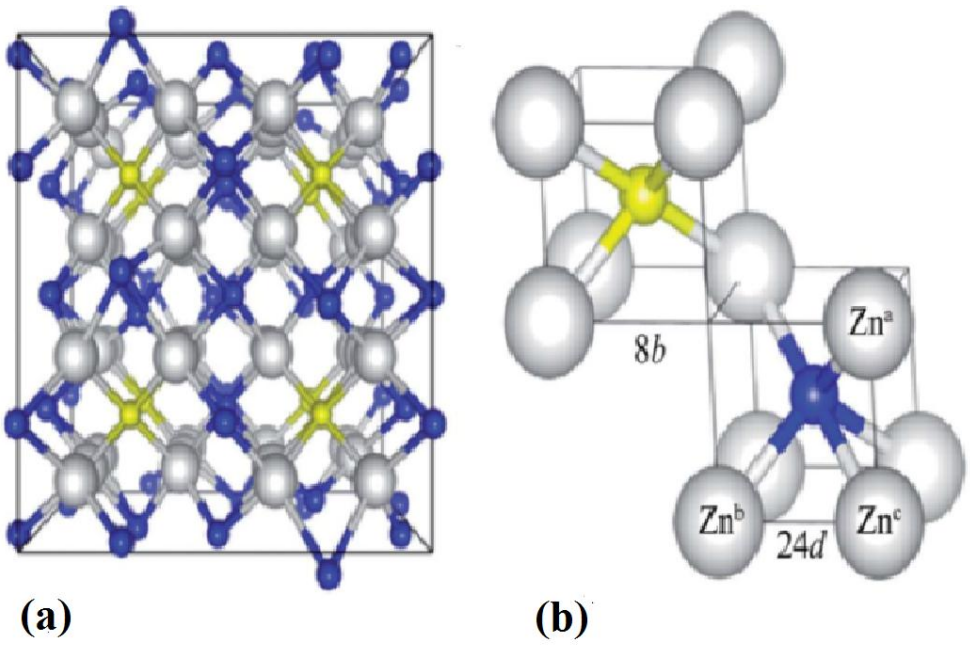

Figure 4-4. (a) Perspective view of the atomic structure of bulk zinc nitride. (b) The arrangement of zinc atoms (as white spheres) around 2 different types of nitrogen atoms as blue and yellow spheres in 8b and 24d Wyckoff positions [9].

PXRD measurements were also performed on three different samples of Zn_3N_2 powder to detect oxygen incorporation in zinc nitride as a phase impurity. All of these samples are black in colour but they have different powder diffraction patterns. S1 represents an almost fresh powder of Zn_3N_2. S2 and S3 were exposed to air for one month and more than a year respectively.

Figure 4.5 shows powder X-ray diffraction data for these three samples. All peaks in the S1 sample match the data for Zn_3N_2 powder in the ICDD document. Figure 4.5 (a) indicates S1 consists of Zn_3N_2 powder as a main phase. In the second scan shown in figure 4.5 (b) for sample S2, a small amount of ZnO as an impurity phase is observed due to peak matching with ZnO powder (ICDD: 04-003-2106). The diffraction data for sample S3 is illustrated in figure 4.5 (c). In this pattern (o) represents ZnO peaks. This scan shows that the ZnO peaks are stronger, and the Zn_3N_2 peaks are weaker in S3 than in S2.

From the relative amplitude of the oxide and nitride peaks, the oxygen and nitrogen content in their structure were found. From PXRD patterns, only 2% ZnO was found in the sample S1. The XRD pattern of sample S2 shows 10% of ZnO and 90% of Zn_3N_2 .We found that 22% of ZnO and about 78% of zinc nitride exist after oxidation in the sample S3. According to powder X-ray diffraction measurements, we observed the formation of ZnO as an impurity phase in Zn_3N_2 powder due to exposure to air over a long period of time. These results demonstrate that the exposure of Zn_3N_2 powder to air causes the formation a layer of zinc oxide (ZnO) possibly around the surface of zinc nitride powders. We speculate that the surface oxide inhibits further oxidation. According to the observed oxygen ratio, the oxidation process of zinc nitride powders is slow .The amount of oxidation within these three samples obtained from PXRD is shown in table1.

Table 1. The oxidation content is shown for different zinc nitride powders estimated by PXRD.

Samples	Oxidation
S1(fresh Zn_3N_2 powder)	2%
S2(exposure to air for 1month)	10%
S3(exposure to air for more than1 year)	22%

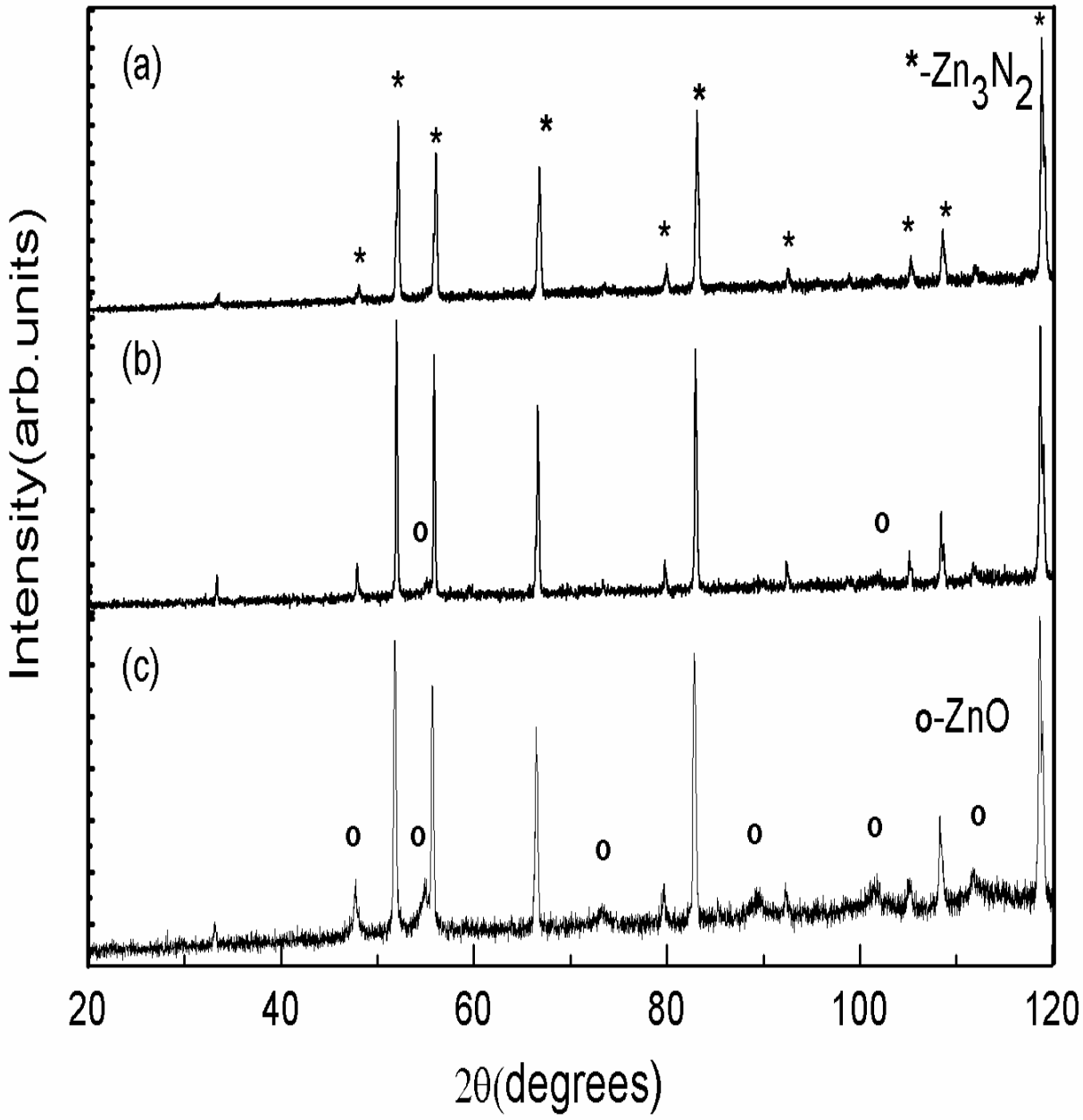

Figure 4-5. XRD patterns: (a) fresh Zn_3N_2 Powder (S1), (b) sample exposed to air for one month (S2), (c) the sample was exposed to air for one year ((o) indicates ZnO peaks)

Photoluminescence measurements

To determine the optical properties of Zn_3N_2 powder, we performed room temperature PL measurements to find out the exact value of the optical bandgap. Room temperature PL measurements were carried out on Zn_3N_2 powder by using two different laser wavelengths in the optical setup. The PL spectrum is illustrated in figure 4.6. The green line spectrum was excited by a 532 nm green laser and has a broad emission centered at 1.15 eV. As shown in figure 4.6, the blue PL spectrum has a peak position at around 1.16 eV which was excited by a 488nm blue laser. The difference is because the blue laser has more excitation energy than green laser.

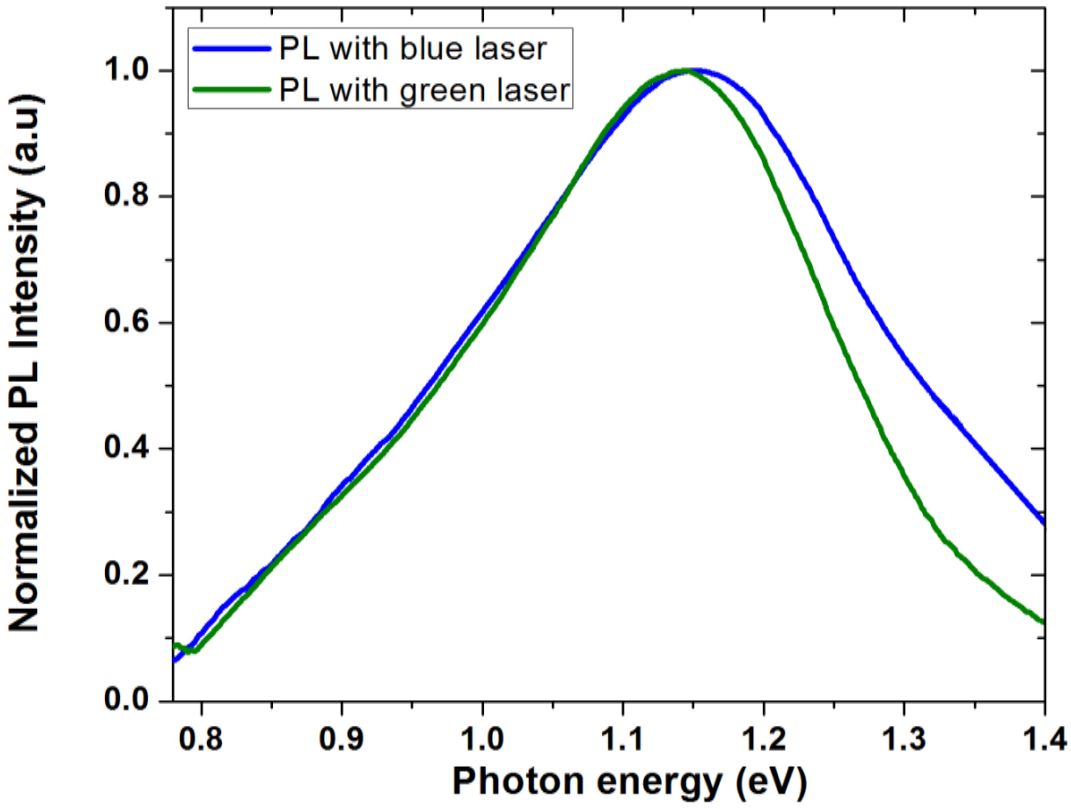

Figure 4-6. Photoluminescence spectrum of Zn_3N_2 powder at RT using different excitation lasers (488nm blue laser and 532nm green laser)

In addition, to have a shorter excitation wavelength, we performed another PL measurement on the same sample with a 345 nm polarized 45 mW He-Cd laser. The PL spectrum shown in

figure 4.7 has a peak emission centered at 1.05 eV. The sharp edge around 0.9 eV is because of using the NIR PMT detector which is sensitive to the range 700-1400 nm shown in fig. 4.7. The bandgap value of Zn_3N_2 powders was found to be around 1.05-1.16 eV using a different PL setup. The difference between PL values might be just because of the oxygen contamination caused by an exposure to air. This value defines the band gap energy of Zn_3N_2 powder which is close to some recent published results. For example in published report [15], they found a bandgap value of 1.06 eV for Zn_3N_2 polycrystalline films from carrier concentration measurements. Paniconi et al. [3] synthesized Zn_3N_2 powders by reacting Zn dust with NH_3 gas at 600^{o}C with a bandgap of 0.9 eV. Another group reported a bandgap value in the range of 1-1.1 eV for Zn_3N_2 nanocrystals which were prepared from the reaction between ammonia and diethyl zinc at 225^{o}C [12].

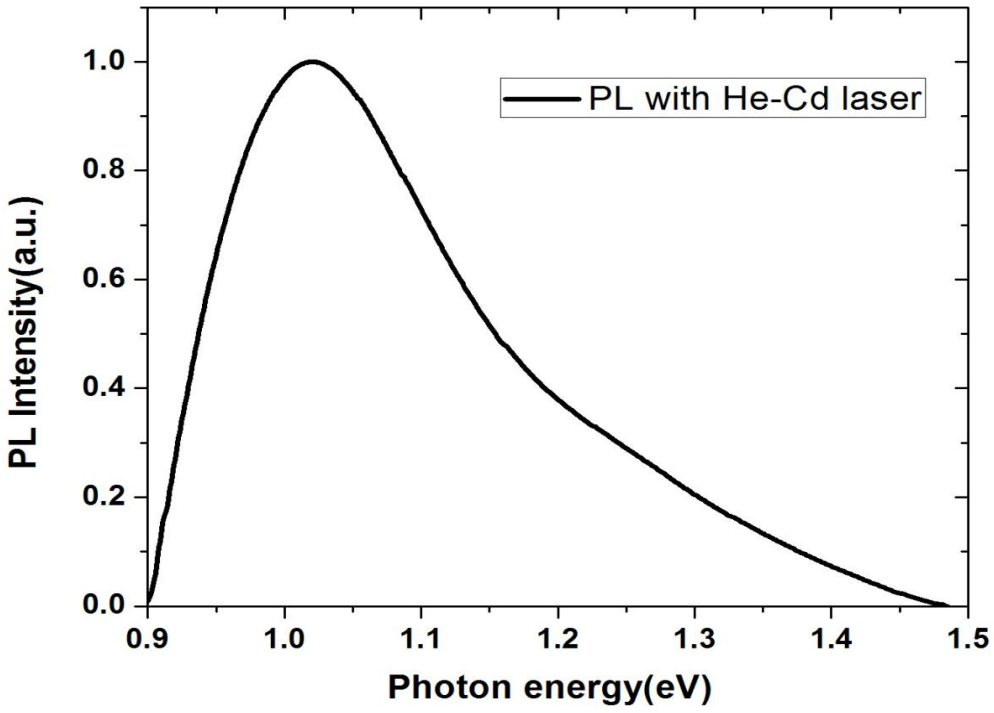

Figure 4-7. Photoluminescence spectra of Zn_3N_2 powder at RT using a 345nm He-Cd laser

Also, low temperature photoluminescence spectroscopy has been done on zinc nitride powder. The resulting spectra have been analysed in order to characterize several features of the crystal including its impurities and defects. The typical low temp photoluminescence spectrum of Zn_3N_2 powder is shown in figure 4.8. As carriers at room temperature can have enough energy to have non-radiative recombination, so, a strong reduction of the intensity of the PL signal would be expected. So by decreasing temperature from 250 K to 10 K, the peak intensity and the energy of the peak both increase. This result agrees with the conventional trend of increasing intensity at low temperature and shows the bandgap has shifted to higher energy by decreasing the temperature. The optical bandgap value is in 0.95-1 eV range in agreement with room temperature PL results.

For the variation of the band gap energy with temperature in semiconductors, different fitting equations have been employed. According to the Bose-Einstein model [26], which relates energy shift to the temperature and the Einstein temperature, the band gap energy as a function of temperature has the following form:

$$E_g\,(T) = E_g(0) - \frac{2\alpha_B}{\exp\left(\frac{\theta_E}{T}\right) - 1} \tag{4-2}$$

where α_B is a parameter associated with the strength of exciton – phonon interactions in the crystal and θ_E is the Einstein characteristic temperature of phonons interacting with the electronic subsystem. $E_g(0)$ is the bandgap energy at T=0 K which can be estimated from the photoluminescence spectrum at low temperatures. The fitting constants are α_B=43 meV and θ_E=340 K for Bose-Einstein function. The Debye temperature [27] can be determined from the relationship: $\theta_D = \frac{4}{3}\,\theta_E$ which is calculated to be $\theta_D = 453$ K. The fitted temperature dependence of the band gap energy in the Bose-Einstein model is illustrated in figure 4.9.

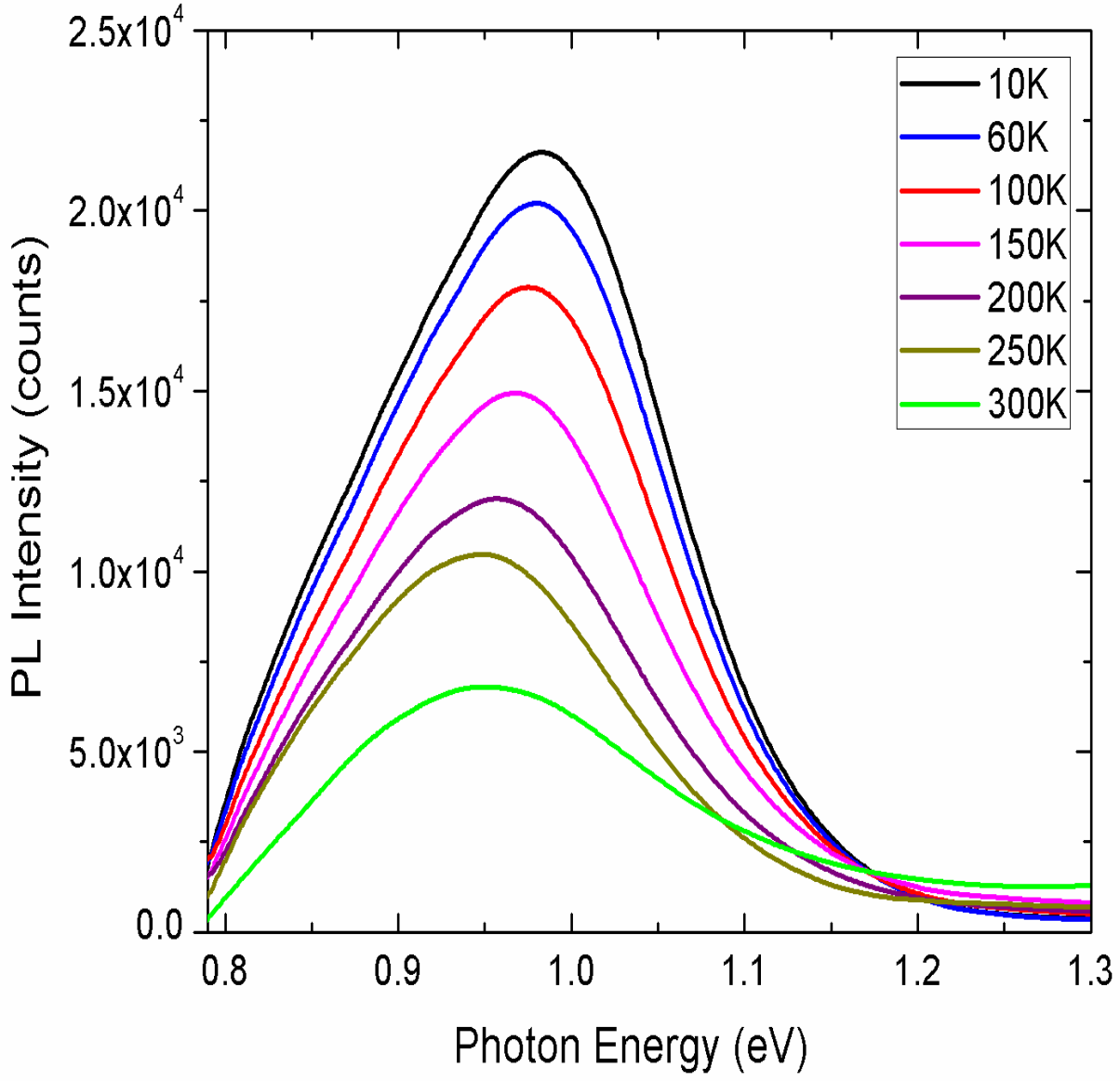

Figure 4-8. Temperature dependence of photoluminescence spectrum for Zn_3N_2 powder

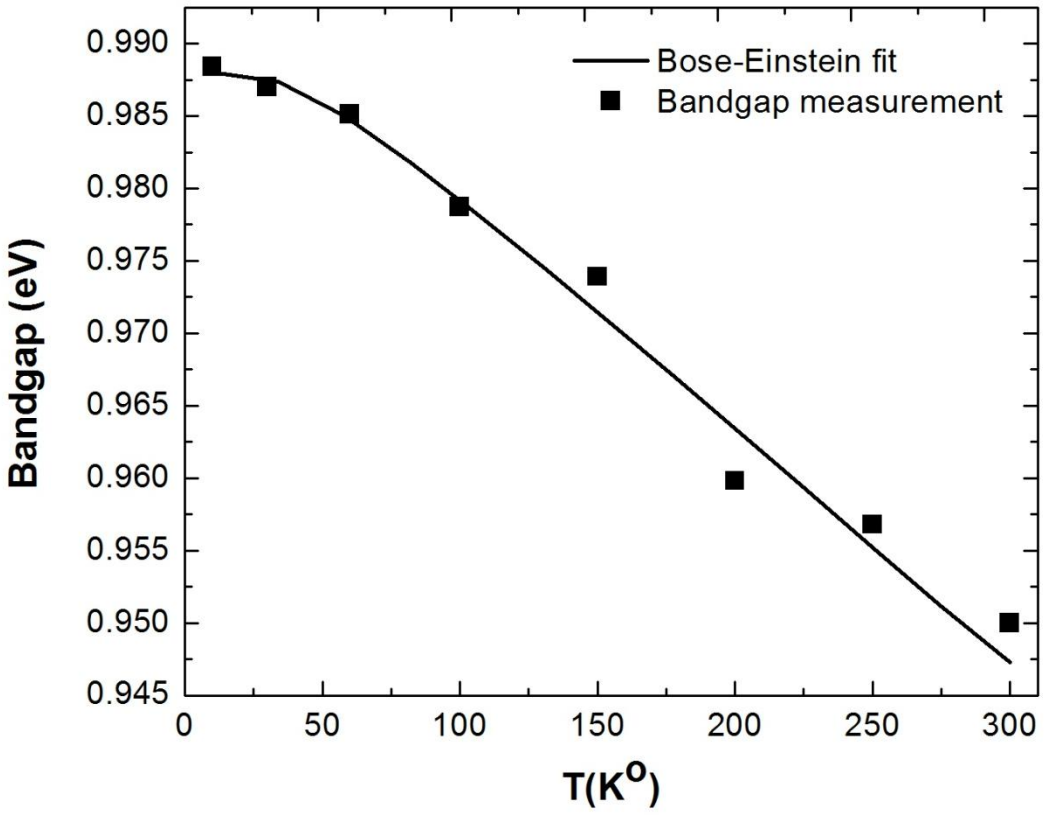

Figure 4-9. Temperature dependence of the band gap energy of Zn_3N_2 powder fitted with the Bose-Einstein equation

Photoluminescence measurements were also performed on three samples (S1, S2, and S3) of Zn_3N_2 powder in order to investigate the effect of oxygen incorporation on the bandgap of zinc nitride. Figure 4.10 shows the PL spectra of these three samples at room temperature. The sample S1 (fresh Zn_3N_2 powder) has a broad peak emission centered at around 1.12 eV. The PL spectrum of sample S2 shows an emission at lower energy, around 0.95 eV at the peak. This peak position is very close to the bandgap of Zn_3N_2 that was calculated to be 0.9 eV by the density-functional theory DFT method [9]. The sample S3 shows 0.85 ev PL emission which is the smallest bandgap reported for Zn_3N_2. Powder XRD measurement of sample S3 verified the existence of oxygen (22%) in its structure after exposure to air for a long time. Therefore, the PL result implies that this emission at 0.85 eV is an oxide-related band transition energy. An energy

gap of 0.9 eV also was found from photoluminescence measurement for the Zn_3N_2 powders prepared by Paniconi et al. [3] through ammonolysis reactions at 600^oC.

Our results show that the oxidation of Zn_3N_2 powder lowers the bandgap energy. One of the most significant problems in the synthesis of Zn_3N_2 powder is that oxygen can easily replace nitrogen and increase its ionic character and apparently reduce its optical bandgap. The reason for the reduction of Zn_3N_2 bandgap because of oxygen contamination will be discussed in more detail in the discussion section.

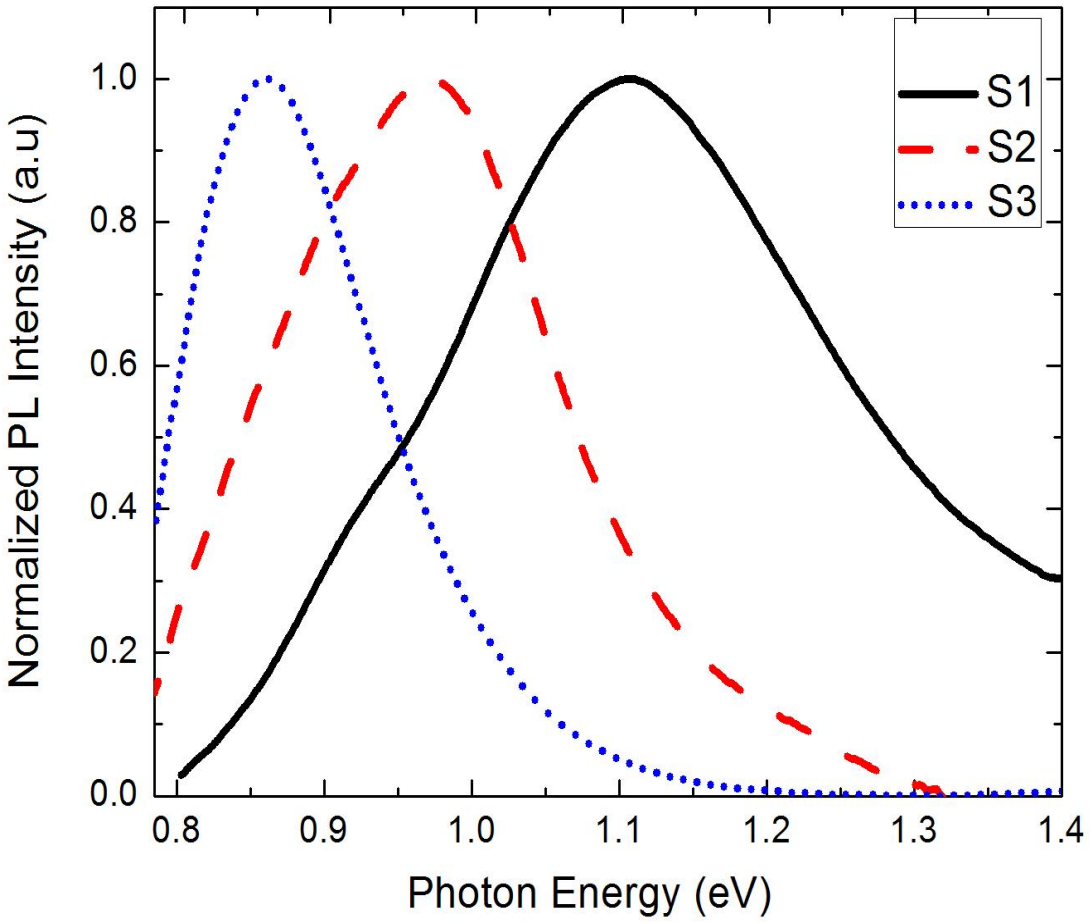

Figure 4-10. The PL spectra at room temperature shows an emission peak at 1.12eV for S1and 0.95eV for S2 and 0.85eV for S3.

Absorption and bandgap measurement

The most significant tools to determine the energy gap of semiconductors is using their optical absorption spectra for which there are different measurement methods. One of the most suitable and simple methods is diffuse reflectance spectroscopy (DR). When a material consists of many particles or nanoparticles, some of the incident light penetrates into sample and the rest gets reflected from the surface. Diffuse reflectance occurs when the incident light returns back from the surface of the sample in random directions [28]. The diffusely reflected radiation collected and detected by the detector is converted into a spectrum. The DRS measurements were carried out on three samples of Zn_3N_2 powder in our optical setup. As mentioned, the sample S1 is fresh Zn_3N_2 powder and S2 and S3 were exposed to air for one month and one year, respectively. The reflectance spectra from the DR measurements are shown in figure 4.11 (a) for the three samples. There are some theories for calculating the optical properties of the material from the diffuse reflectance. The first method was defined by Kubelka and Munk [22, 23] in 1931. According to the Kubelka-Munk (K-M) theory, the diffuse reflection occurs when the particle size is equal to or smaller than the wavelength of incident light. Furthermore they assumed the material is isotropic and homogeneous to be capable of scattering the light. They also supposed that there are no specular reflection and boundary effects. In the Kubelka-Munk function

$$F(R_\infty) = (1 - R_\infty)^2 / 2R_\infty = k/s \tag{4-3}$$

s and k are called K-M scattering and absorption coefficients, respectively. Now by using $F(R_\infty)$, we can get k as a K-M absorption coefficient from the diffuse reflectance result. The KM absorption spectra of three samples are shown in figure 4.11 (b).

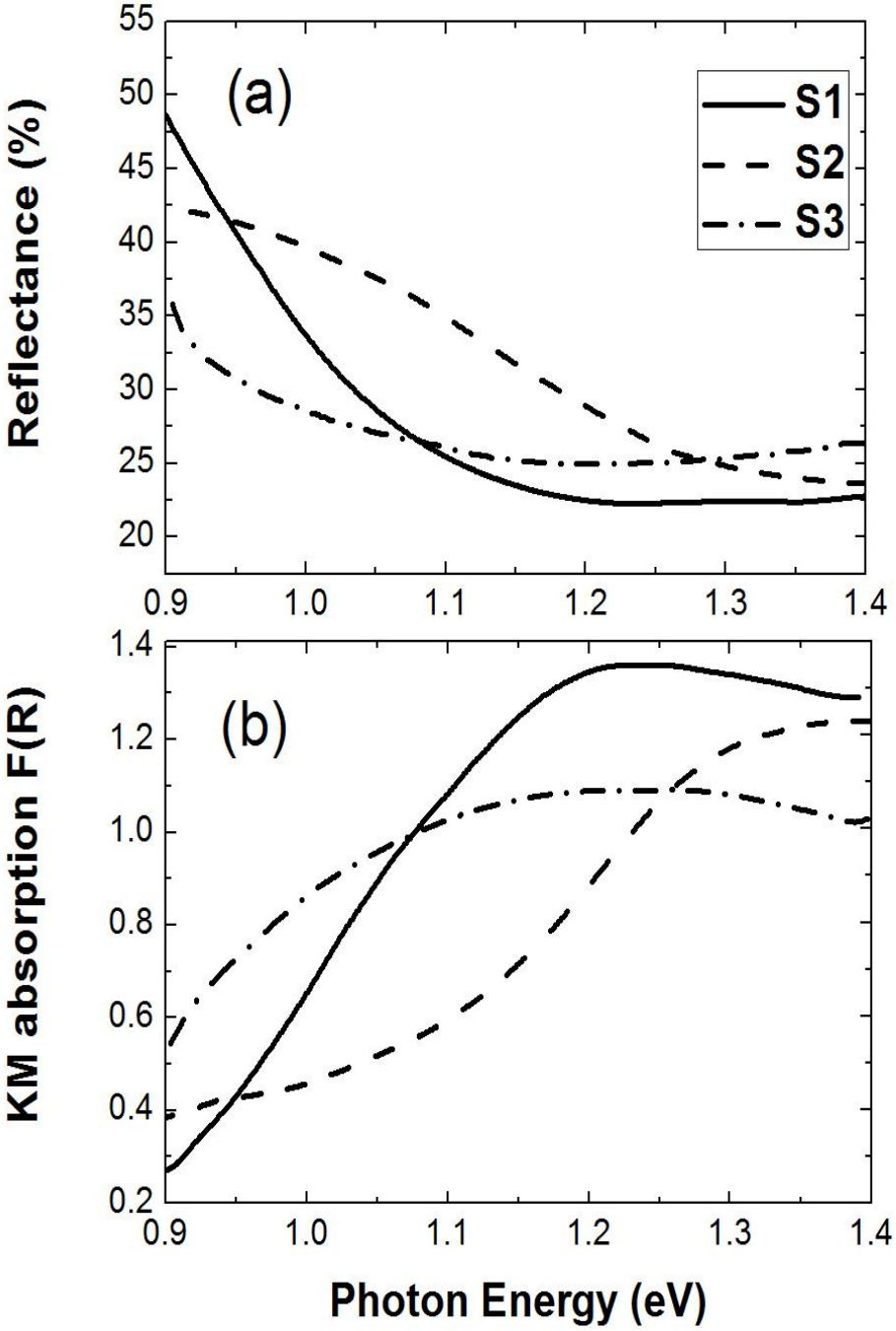

4-11. Plot (a) is reflectance spectra of samples S1, S2, and S3 and plot (b) is Kubelka-Munk transformed reflectance spectra or KM absorption coefficient of S1, S2, and S3

The K-M absorption spectrum was used to evaluate the bandgap energy of Zn_3N_2. The K-M scattering coefficient s is assumed to be constant with respect to wavelength close to the bandgap. To optimize the diffuse reflectance signal, the beam was incident on the surface of the sample at a 30^o angle from the normal and the detector was placed at the specular position. Because the powder doesn't have any specular reflection this alignment gives the maximum diffuse reflection signal. On the other hand, when the material is in the maximum diffuse position, the K-M absorption coefficient k becomes equal to 2α [23] where α is the linear absorption coefficient of the material. So $F(R_\infty)$ is clearly proportional to the absorption coefficient. To investigate the absorption edge of a direct bandgap semiconductor, Eq.4.4 is used:

$$(\alpha h\nu)^2 = C1\left(h\nu - E_g\right) \tag{4-4}$$

By assuming the optical bandgap for Zn_3N_2 is direct as indicated in published reports in [4, 7, and 29], we can use this equation to get its bandgap with the help of Eq.4.5:

$$[F(R_\infty)h\nu]^2 = C1\left(h\nu - E_g\right) \tag{4-5}$$

Therefore, by using $F(R_\infty)$ as an absorption coefficient, the optical band gap E_g of a Zn_3N_2 powder can be extracted easily through plotting $[F(R_\infty)h\nu]^2$ versus $h\nu$. The corresponding plots are shown in figure 4.12. The energy of the optical band gap was found by extrapolation of the linear portion to the energy axis (hν). So, via this method the calculation of band gap can be made more accurate. The optical bandgap of S1 is calculated to be 1.12 eV and this matches with our result from the PL measurement. Besides, our group in [16] reported the bandgap value of 1.25 eV for the single crystal zinc nitride films using transmittance measurements. The value of the energy gap for S2 is estimated to be about 0.98 eV from the data in figure 4.12 which is the same as the corresponding PL result. This value is also close to the result which was published in

[30]. They used transmittance spectra to find the optical bandgap to be around 1.01 eV for Zn_3N_2 films which were prepared by RF sputtering. Also in 2005, Toyoura et al. [29] prepared zinc nitride films using molten salt electrochemical process and reported the bandgap to be 1.01 eV from reflectance measurements. Similarly, the bandgap of S3 is approximately 0.85 eV. Due to same results from PL and DR, we conclude that these values provide reliable measurement of the optical bandgap of zinc nitride powders. In addition, these measurements show that the optical bandgap of Zn_3N_2 is reduced by oxygen incorporation.

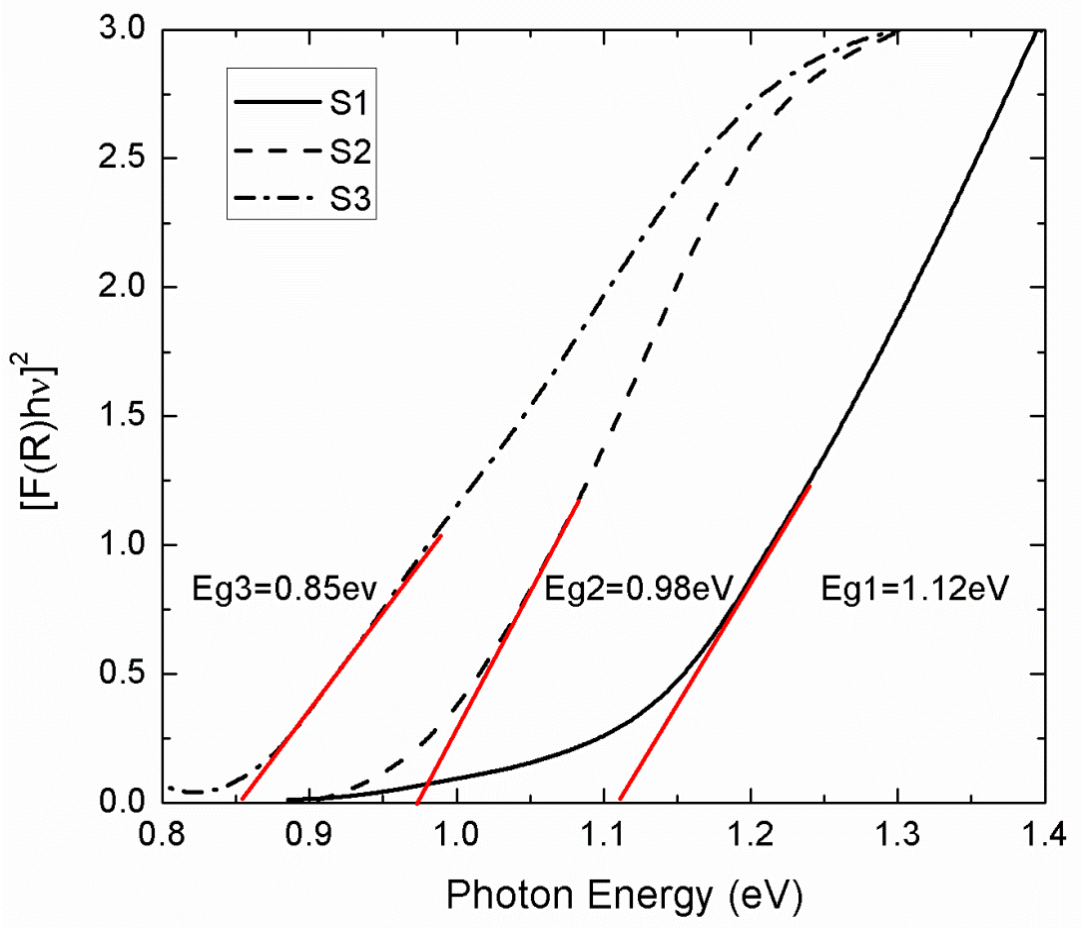

4-12. A plot of $[\boldsymbol{F}(\boldsymbol{R}_\infty)\boldsymbol{h\nu}]^2$ as a function of photon energy for three different samples of Zn_3N_2 powder.

Furthermore, to test the accuracy of the DR method, some extra UV-Vis absorption spectroscopy was done on silicon powder, which has a known bandgap in the same energy range and on Zn_3N_2 powder sample S3. The Perkin Elmer lambda 1050 model UV-Vis spectrometer was used to characterize light absorption properties of the pellet form of these powders. The UV-Vis absorption spectrum of a silicon powder is shown in figure 4.13. From this spectrum the indirect bandgap energy of Si from UV-Vis absorption spectroscopy is estimated to be 1.04eV. On the other hand, the KM bandgap value was calculated to be 1.04 eV for silicon powder from the DR measurements illustrated in figure 4.14. In the same way, for sample S3 a bandgap energy of 0.78 eV was assessed by using its UV-Vis spectrum presented in figure 4.15. Our results obtained from samples indicate that, the DR technique (our setup) is consistent with the UV-Vis absorption technique in extracting the band gap values of powder semiconductors. The UV-Vis spectrometer couldn't be used for other samples because the light source of the spectrometer was broken.

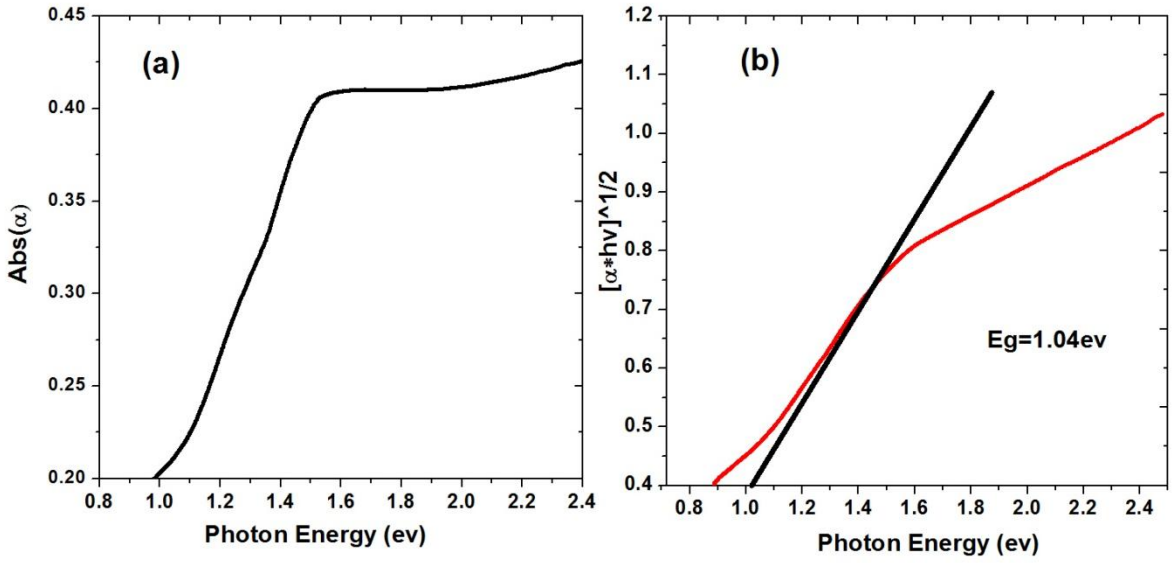

4-13. UV-Vis spectroscopy of silicon results having bandgap energy of 1.04eV

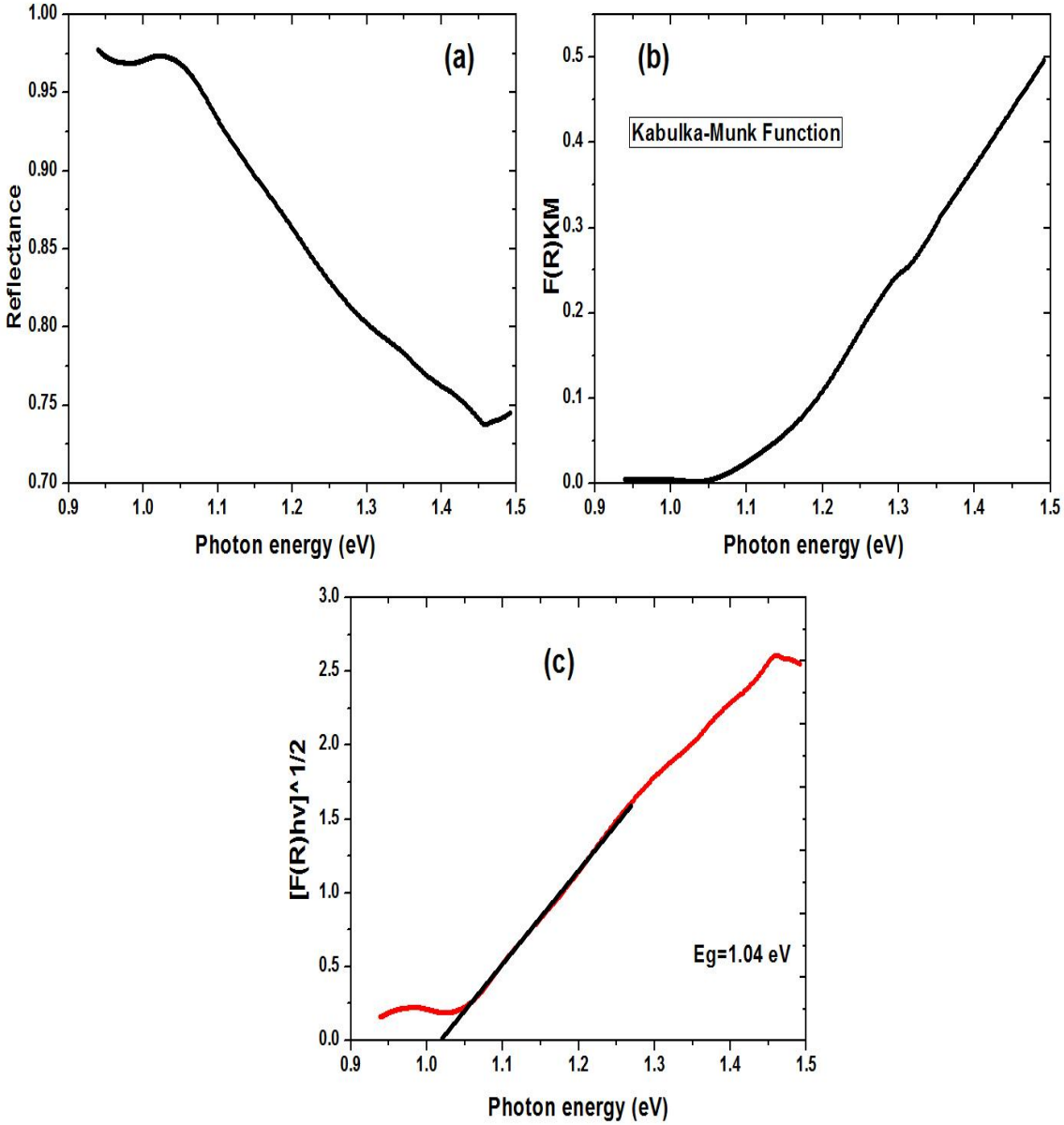

Figure 4-14. Diffuse reflectance spectrum of silicon powder confirms the bandgap energy value around 1.04eV.

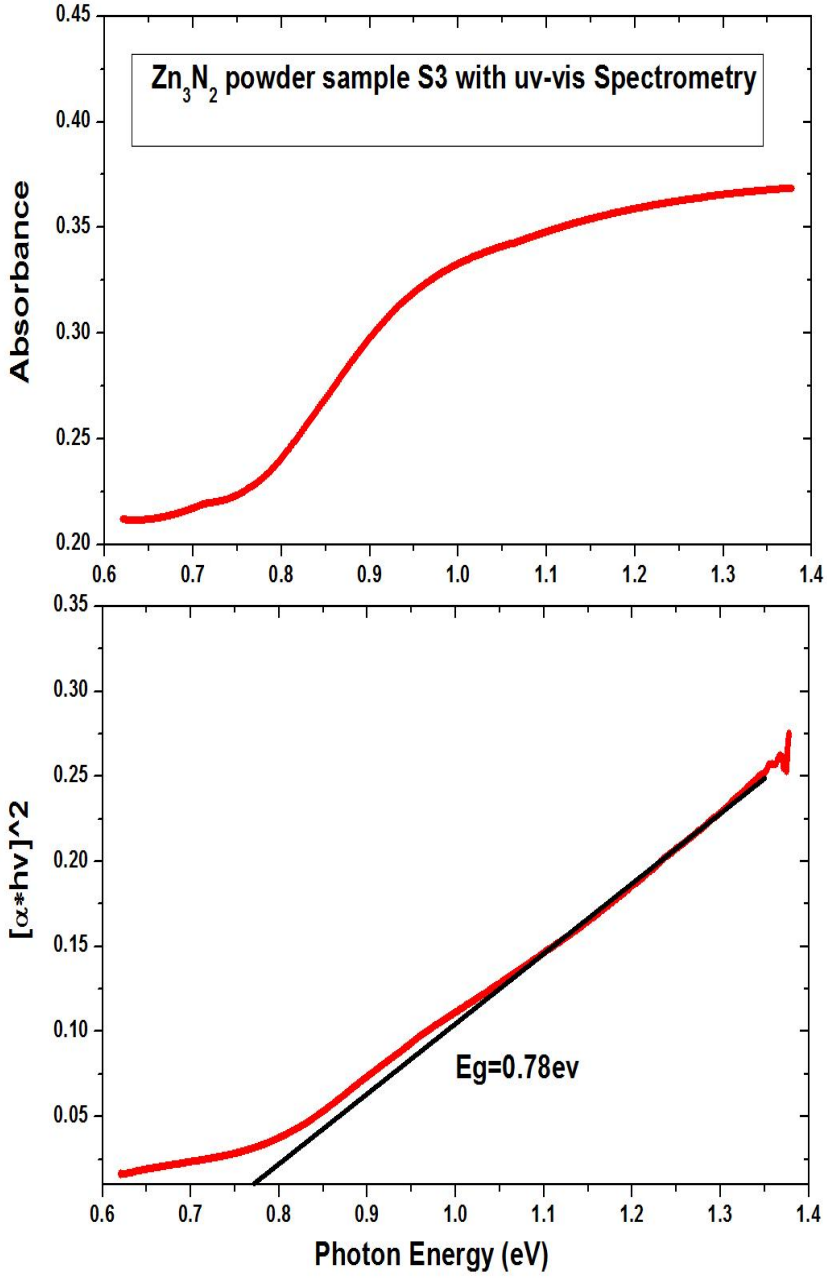

Figure 4-15. UV-Vis spectroscopy of sample S3 indicates the bandgap energy of 0.78 eV which is close to our DR result

Thermal nitriding effect on the bandgap energy

We used thermal nitriding to study the effect of varying the ZnO/Zn_3N_2 ratio on the bandgap energy of Zn_3N_2 powder. The nitriding process was performed when oxidized Zn_3N_2 powders were heated up inside the furnace and exposed to ammonia gas. To determine the oxygen/nitrogen ratio, powder XRD measurements were carried out on this oxidized zinc nitride powder. The PXRD analysis of the oxidized Zn_3N_2 powder indicates that the O/N ratio is 45% before nitriding. The sample S4 is the new powder sample obtained after the thermal nitriding process. In order to determine the optical bandgap energy, PL measurements were performed on these powders. The PL spectra for this powder after and before the thermal nitriding are shown in figure 4.16. The PL spectra indicate that annealing the partially oxidized powder in ammonia atmosphere at $500C^{o}$ for 2 hours, shifts the PL emission peak from 0.85 eV to 1.2 eV. Also, the PXRD pattern of sample S4 describes how the oxygen/nitrogen ratio decreased from 45% to 32% after thermal nitriding. As mentioned in some published reports, doping nitrogen into zinc oxide material can lower the optical bandgap value of ZnO [32] because of the higher p orbital energy for nitrogen in the valence band. In this study, we found that adding O to Zn_3N_2 reduces the bandgap and also that increasing N in oxidized Zn_3N_2 increases the bandgap. The bandgap of $Zn_3 (N_{1-x} O_x)_{2-y}$ was reported at [31, 33] to be in the range of 1.2-1.3 eV, differing depending on the oxygen-nitrogen ratio. The value of x was reported in [33] to be around 0.11 to have a bandgap energy of 1.2 eV for $Zn_3 (N_{1-x} O_x)_{2-y}$ structure which is same as our obtained bandgap value. Also there is another group who found a larger bandgap around 2.5 eV due to different oxygen ratio within $Zn_3N_{2-x}O_x$ structure [42]. The different bandgap energies obtained from our results and other published values are listed in Table 2 which shows how the oxygen ratio can change the optical bandgap of Zn_3N_2 material.

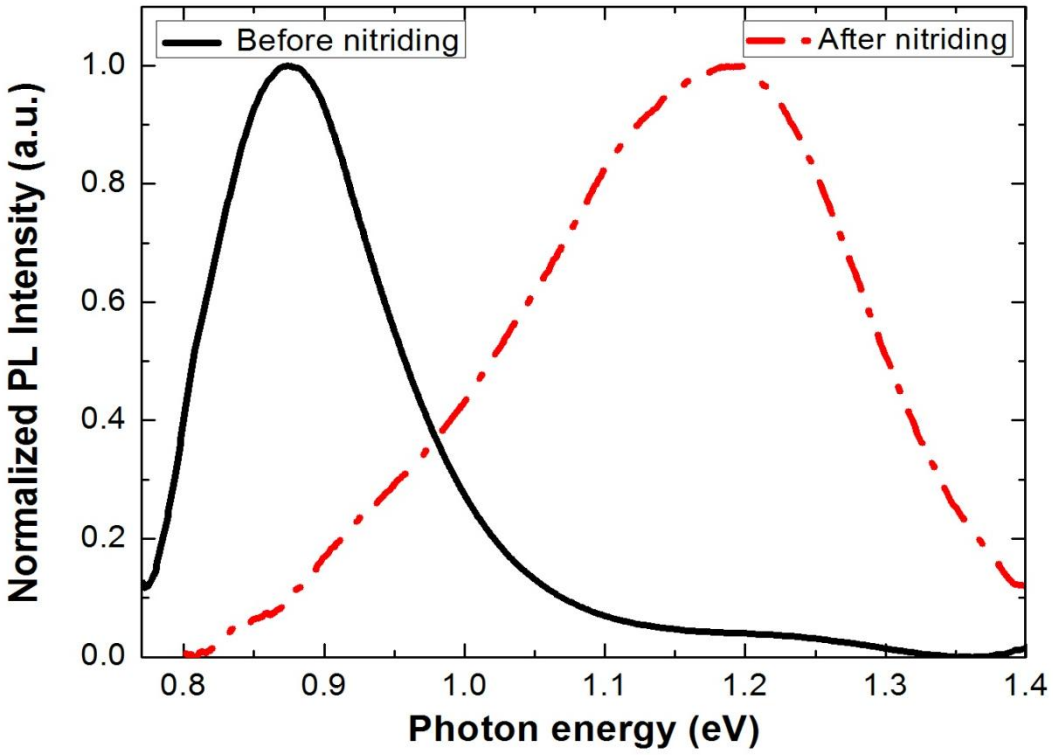

Figure 4-16. The PL spectra of the oxidized Zn_3N_2 powder has an emission centered at 0.85eV and 1.2eV after thermal nitriding process

Table 2**.** Optical band gaps extracted from PL spectra and other published values. The percentage of O atoms within different zinc nitride powders was estimated by PXRD.

Samples (condition)	O ratio (%)	Optical bandgap E_g(eV)
S1(fresh Zn_3N_2 powder)	2%	1.12
S2 (exposure to air for 1month)	10%	0.98
S3(exposure to air for more than1 year)	22%	0.85
S4 (oxidized Zn_3N_2 powder after nitriding)	32%[1]	1.2
Zn_3N_2 films [16]	----	1.25
$Zn_3N_{2-x}O_x$ [42]	----	2.5
$Zn_3(N_{1-x}O_x)_{2-y}$ [33]	----	1.2-1.3
Zn_3N_2 films [4,43]	----	3.4
Zn_3N_2 films [31]	----	1.5

1. The oxidized Zn_3N_2 powder had 45% O/ (N+O) ratio before nitriding process which is decreased to 32% after nitriding.

Thermal oxidation of zinc nitride powder

Thermal oxidation of zinc nitride powder was performed at temperatures from 200 to 700 °C for 2 hours. XRD scans for samples oxidized at different temperatures are shown in figure 4.17. XRD patterns can be analyzed by measuring the intensity of the peak and also the peak position. Both pieces of information are included in the ICDD document. The PXRD scans demonstrate how the peak position changes at different annealing temperature. According to the Scherrer equation [45], the peak width is inversely proportional to the crystallite size, meaning that narrow peaks correspond to larger crystallites while broader peaks are attributed to smaller crystallite size. Peak width or full-width-at-half-maximum (FWHM) was determined for ZnN and ZnO powders using PXRD patterns. The mean crystallite size of the sample is evaluated by means of the Scherrer formula:

$$D = \frac{0.9\lambda}{B(2\theta) * cos\theta_B} \quad (4\text{-}6)$$

where λ, θ_B and B are the X-ray wavelength (0.1542 nm), Bragg diffraction angle and the peak width respectively. According to the peak width, the crystallite size was estimated to be 45nm for ZnN (400) and 15nm for ZnO (101). The high intensity narrow peaks for ZnN powder correspond to large particles while the wide peaks for ZnO powder correspond to smaller particles. According to the XRD patterns for samples annealed from 200^o to 400^o C, zinc nitride peaks didn't differ much and no zinc oxide appeared in the material. According to the fact that the material annealed from 200^o-400^oC, contains less than 10% ZnO it can be concluded that there was just some limited surface oxidation. The formation of ZnO on the surface of the ZnN particles may protect the interior of the zinc nitride powders from bulk oxidation. According to our results, the thermal oxidation of zinc nitride powders in the 200^o-400^oC range is a slow process. When the temperature is higher than 500^oC, fast thermal oxidation occurs on the

exterior of zinc nitride powder. Zinc oxide peaks started to appear and continuous heating at higher temperatures causes a transformation to pure ZnO. This is also clearly shown in figure 4.18 namely that the intensity of the zinc nitride peaks decreases with increasing temperature. The PXRD data of Zn_3N_2 powder through thermal oxidation in air at different temperatures proved that bulk oxidation of the Zn_3N_2 powders occurred above 500 ^oC.

Thermal gravimetric analysis in [34] also showed that the thermal decomposition behaviour of Zn_3N_2 powder is fast above 500 ^oC similar to our thermal oxidation result.

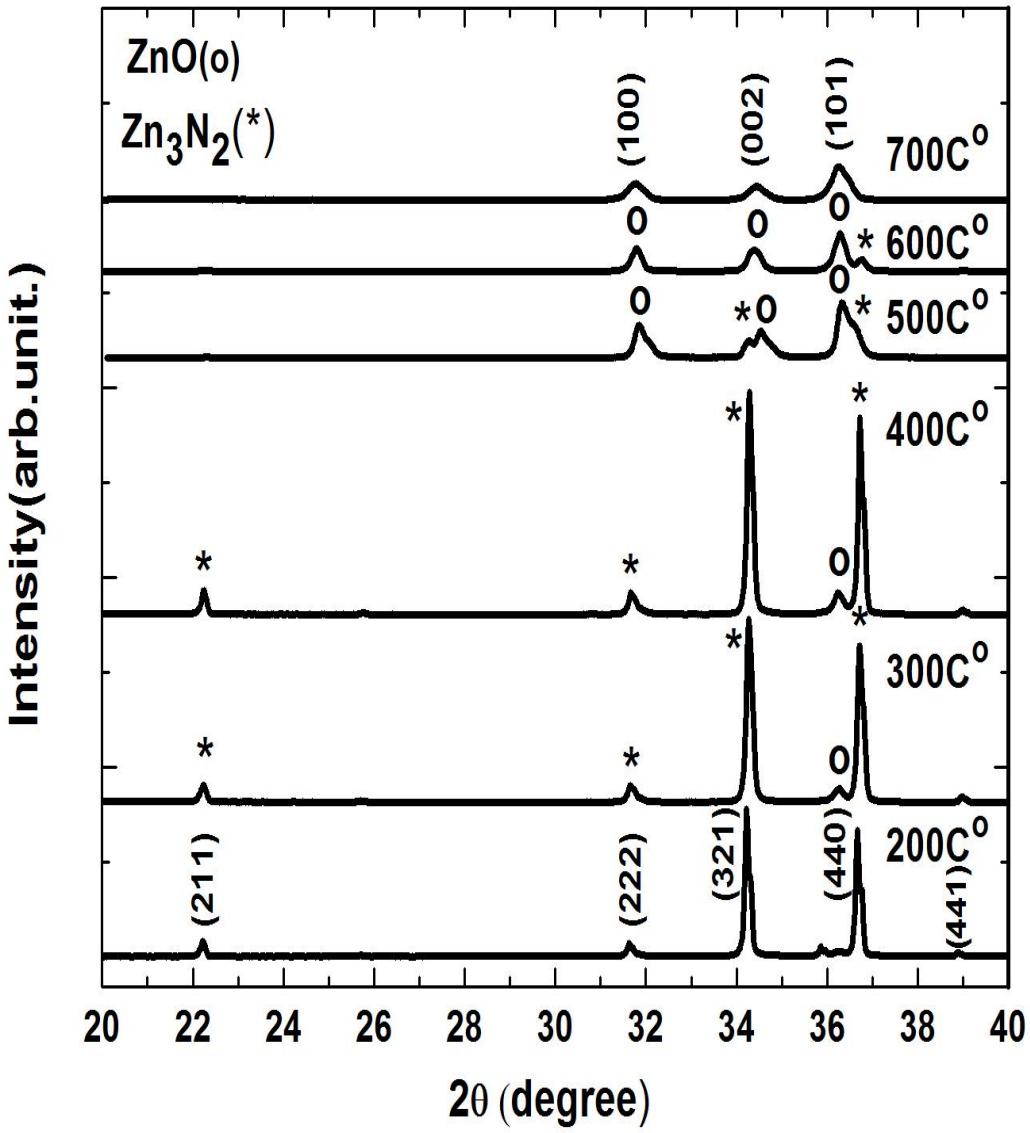

Figure 4-17. Powder X-ray diffraction patterns following thermal oxidation of Zn_3N_2 powder for 2 hours at temperatures between 200° and 700°C.

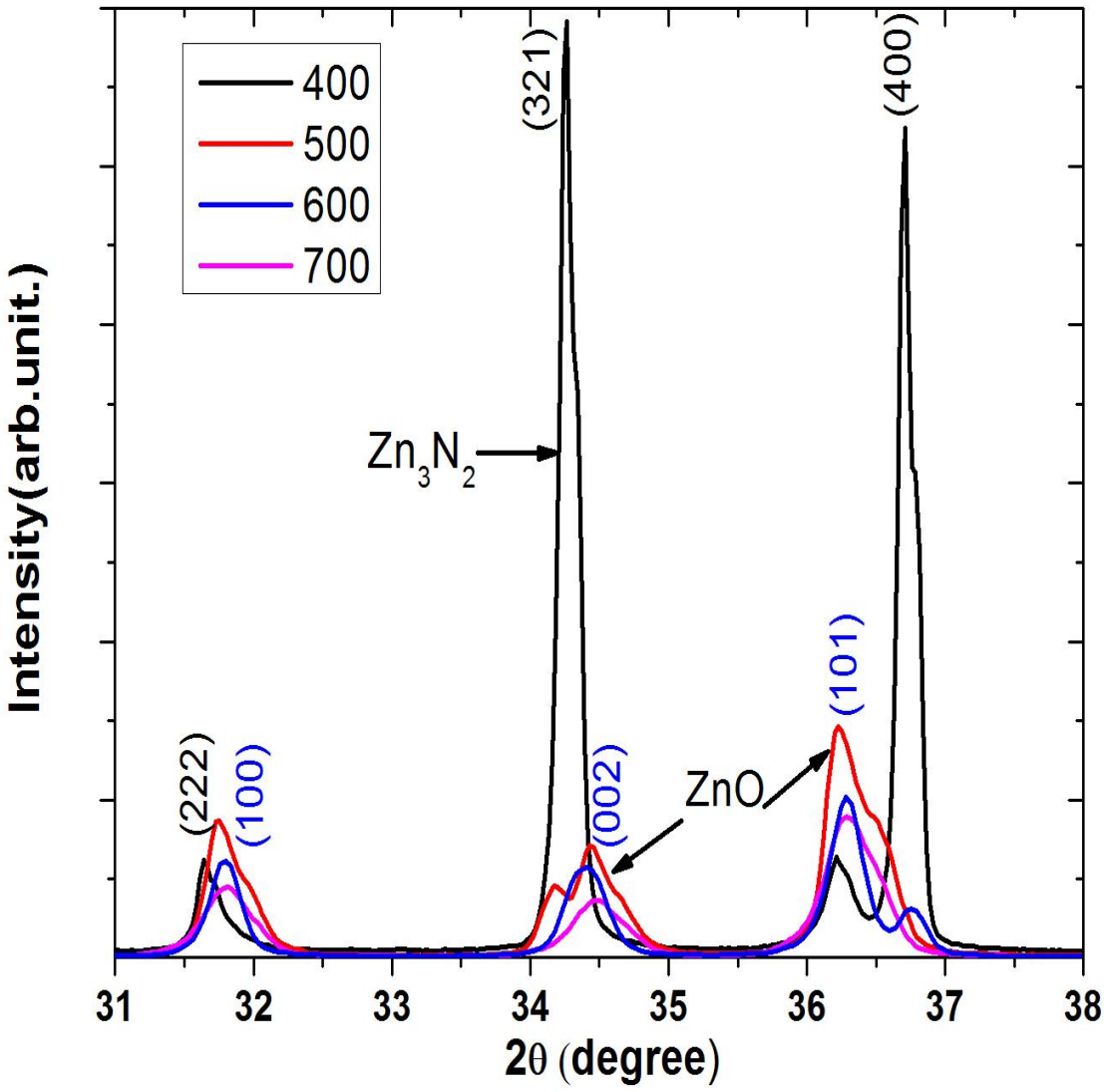

Figure 4-18. Powder X-ray diffraction patterns following thermal oxidation of Zn_3N_2 powders at temperatures between 400°-700°C in the 2θ range from 31° to 38°.

The quantity of Zn_3N_2 powder annealed in air at a temperature from 200^o to 700^{o}C was found. These values were obtained by the peak fitting using ICDD data. By comparing the peak intensity of ZnO and Zn_3N_2 in PXRD pattern shown in figure 4-17, the quantity of these powders could be found at each temperature separately. Consequently, powder XRD scans can be used to estimate the concentration of ZnO within the Zn_3N_2 powder as a function of annealing. The total amount of Zn_3N_2 and ZnO at different temperature is plotted in figure 4.19. This data was fitted with the logistic function by using Eq.4.7:

$$f(T) = \frac{1}{1 + Be^{\frac{-E_a}{KT}}} \tag{4-7}$$

where *f (T)* describes the decline of Zn_3N_2 as a function of temperature, and E_a is an activation energy while B is a dimensionless constant. Eq.4.7 was used to fit the data showing exponential decline of the Zn_3N_2 concentration as a function of temperature from 200^o to 700^{o}C as shown in figure 4.19. Additionally to fit the equation to the exponential growth of ZnO, the other logistic equation was applied:

$$f(T) = \frac{Be^{\frac{-E_a}{KT}}}{1 + Be^{\frac{-E_a}{KT}}} \tag{4-8}$$

where *f (T)* describes the exponential growth of ZnO as a function of temperature as shown in figure 4.19 with circular points. From the fits to the experimental data, the activation energy of this reaction is determined to be 0.7 eV. This means the growth of the oxygen-nitrogen ratio (O/N) through the oxidation of Zn_3N_2 depends on temperature and slows down below 400^{o}C. This result indicates that Zn_3N_2 powders are relatively stable at room temperature and oxidize slowly.

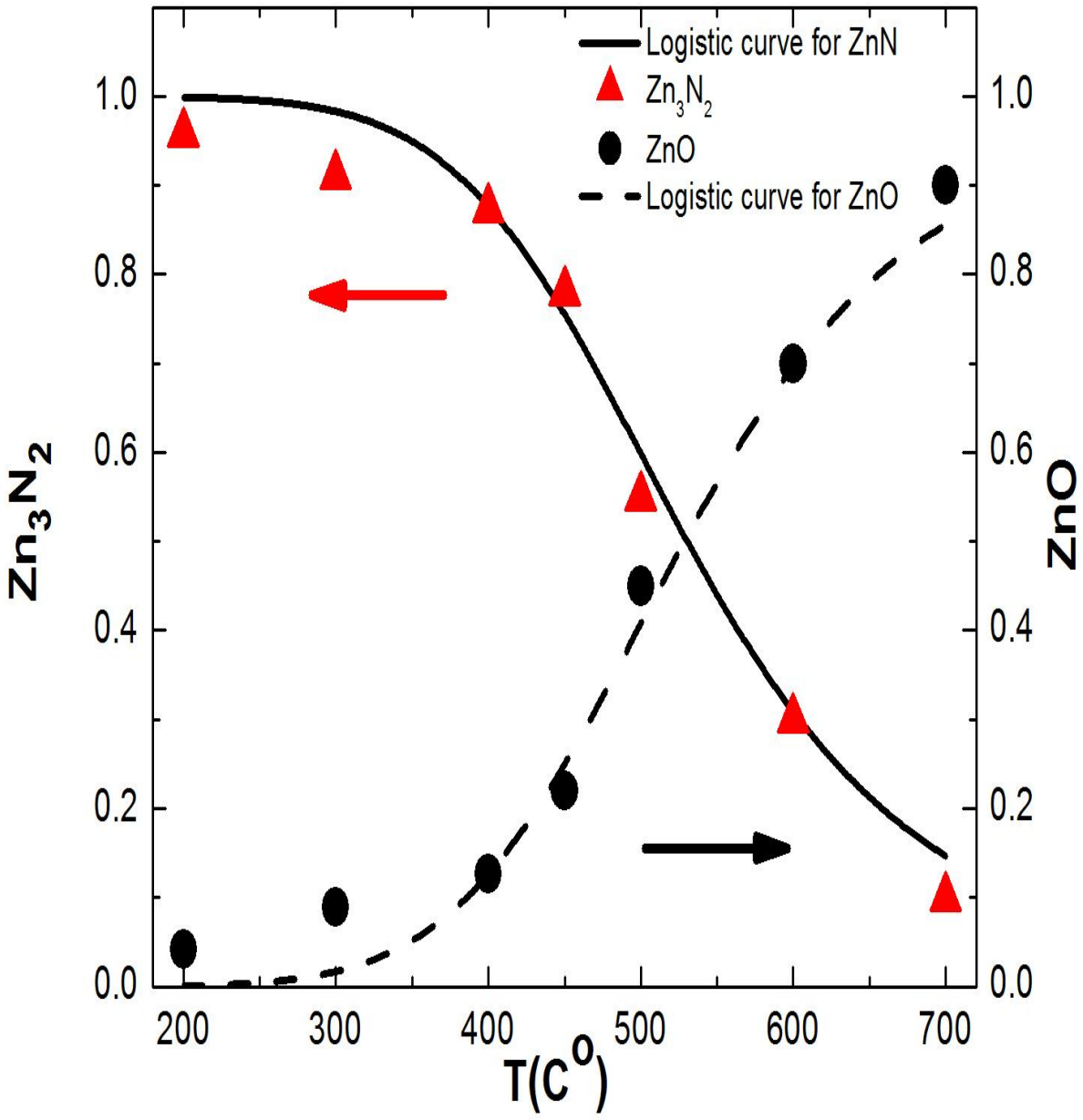

Figure 4-19. Triangular points and circular points show the quantity of Zn_3N_2 and ZnO at different temperature respectively. The lines are logistic curves fitted to the experimental data

To observe the bulk oxidation of Zn_3N_2 powder, the annealing temperature was set at 500^oC and the Zn_3N_2 sample was annealed for progressively longer times up to 6 hours in an ambient air. Figure 4.20 shows the XRD patterns of zinc nitride powder after thermal annealing in air for different lengths of time. According to the PXRD patterns, under this experimental condition, after 6 hours annealing in air the sample was mostly converted to ZnO (more than 70%). This is evident in the PXRD pattern in figure 4.20 in which ZnO peaks such as (100), (002) and (101) are dominant in this 2θ range. After 6 h annealing in air, almost complete oxidation occurred and the main Zn_3N_2 peaks such as (321) and (400) completely vanished.

This can also be credited to the fact that after annealing powder in air at 500^oC and consequently doping with the oxygen, the FWHM will increase in the crystalline structure as shown in PXRD scans in figure 4.20. On the other hand, due to formation of the ZnO, the Zn_3N_2 particles will shrink. The diminishing of the zinc nitride peaks is clearly shown in PXRD scans in figure 4.21. It indicates the disappearance of the (321) plane of zinc nitride structure located near $2\theta = 34^o$ due to thermal annealing. Also this diffraction data shows that the ZnO (002) reflection peak positioned at $2\theta = 34.30^o$ is growing with time.

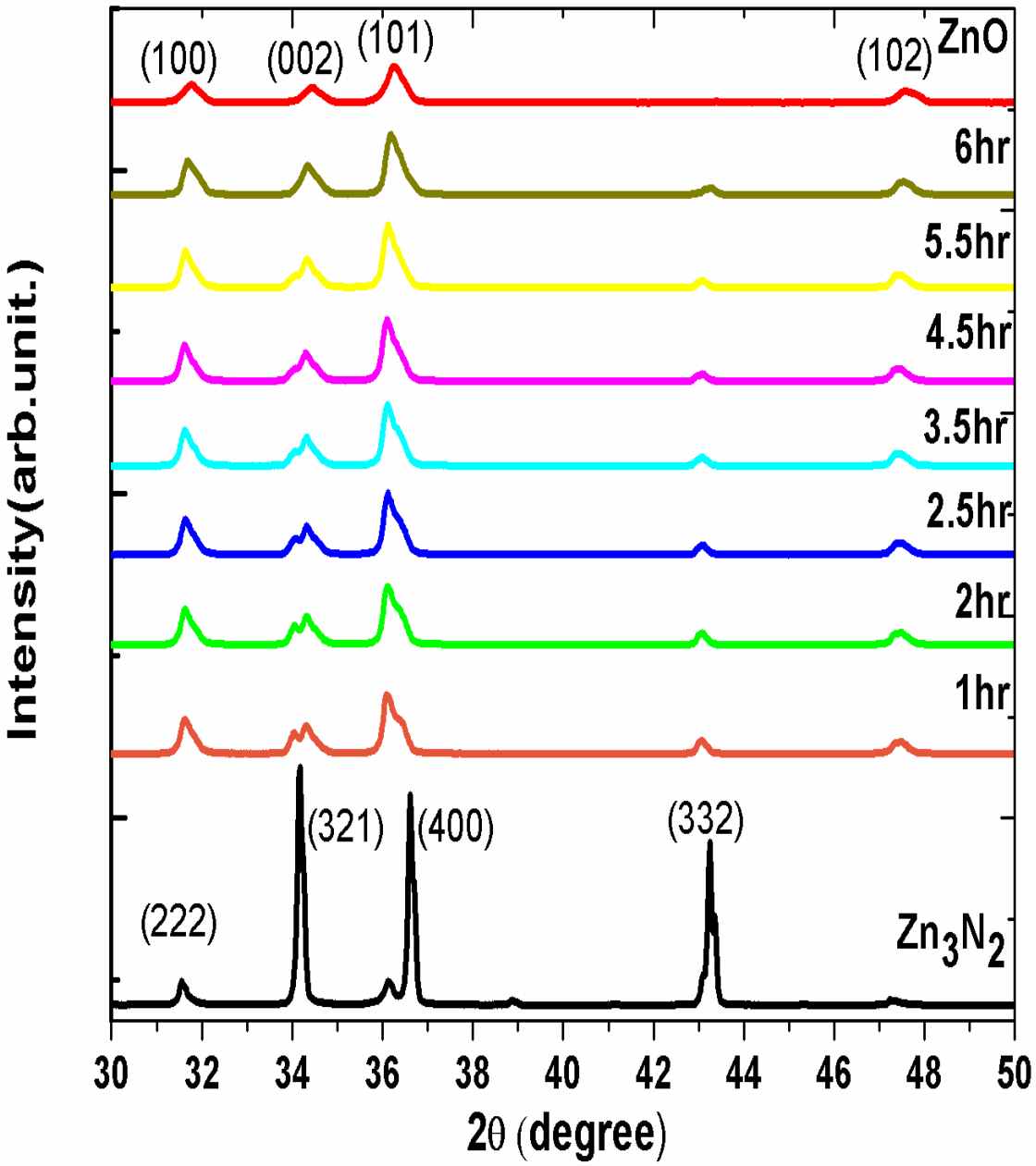

Figure 4-20. X-ray diffraction patterns of zinc nitride powder after thermal oxidation in air at 500°C for different lengths of time.

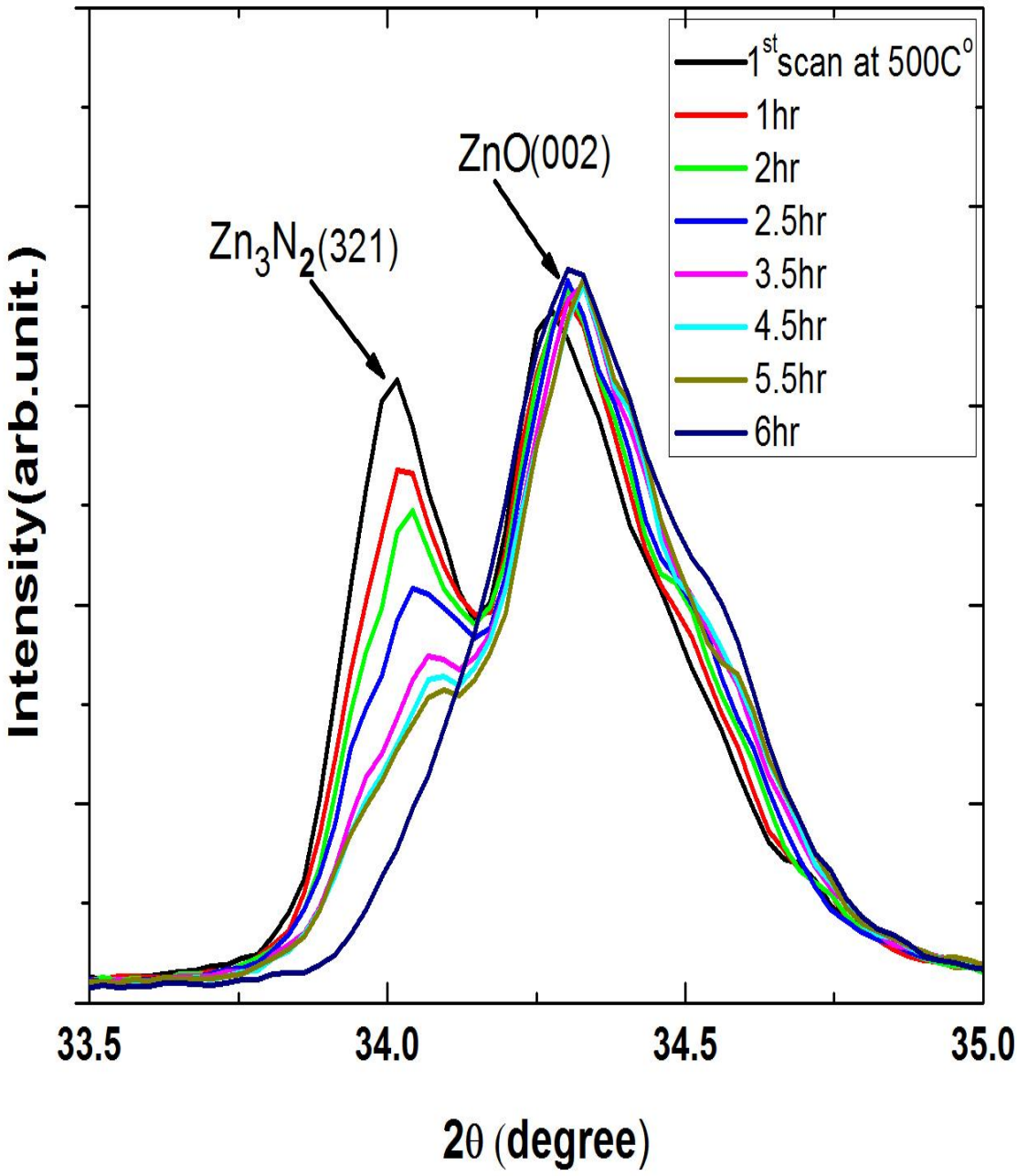

4-21. Expanded (321) peak of Zn_3N_2 and (002) peak of ZnO in air-annealed zinc nitride powder

5. Discussion

From the literatures, it is clear that the band gap and optical properties of Zn_3N_2 are related to the composition of the material. From our measurements, the optical bandgap value was found to be ~1.2 eV for zinc nitride powder. In this study, all data from PL and DR measurements indicates that the bandgap of Zn_3N_2 powder decreases due to the oxidation. The uncertainty in the literature regarding the bandgap of Zn_3N_2 may be due to uncontrolled O contamination. Because it would be expected by increasing the oxygen the bandgap of material would be increased. The reduction of the optical bandgap of Zn_3N_2 films was also reported in [35] in the case of thermal annealing. On the other hand, some literature reported that oxygen incorporation results in the enhancement of both the ionic character and band gap energy, respectively [31, 32]. Additionally, DFT calculations in [36] verified that substituting O for N atoms produces more stable composition within the anti-bixbyite zinc nitride. A possible explanation for the reduction of Zn_3N_2 bandgap by oxygen substitution is related to the band anti-crossing (BAC) model of highly mismatched semiconductor alloys (HMAs) [37]. The electronegativity of nitrogen is 3.0 which is less than 3.4 the electronegativity of oxygen [38]. This means that anti-bonding states of the oxygen impurity atoms can be located near and below the conduction band since the oxygen has greater electronegativity than the nitrogen. These localized states of oxygen below the conduction band edge will lead to the formation of a narrow intermediate band. The energy sub-band formation inside of the bandgap due to the oxygen incorporation also was observed for hexagonal boron nitride (BN) in [41]. From our results we conclude that this sub-band is responsible for the reduction of the zinc nitride bandgap as long as there is only a small amount of oxygen incorporation. The oxygen impurity levels in II-VI semiconductors have also been studied lately. According to these experimental studies, if the electronegativity of the anion impurity is much larger than the host atom e.g., GaP:N and ZnTe:O, the anion impurity level will

form near the conduction band minimum CBM [46]. Additionally, a wide lower sub-band is formed within the conduction band of CdTe by oxygen incorporation which consequently caused a reduction of the band gap energy [40]. Also, narrowing of the bandgap due to the oxygen incorporation has been reported for ZnO_xSe_{1-x} by anti-crossing model [39].

Figure 5.1 is a schematic energy diagram for the interpretation of bandgap reduction results from PL and DR measurements. According to this schematic, the incorporation of oxygen can make an intermediate impurity band within the bandgap of zinc nitride which can slightly decrease the bandgap energy. The O2s anti-bonding level close to the bottom of the conduction band pushes the CB down. Also, the O2s bonding orbital forms in the valence band. If the oxygen content increases further within the Zn_3N_2 structure, the bandgap energy will eventually increase. In figure 5.1 the optical bandgap energies for pure Zn_3N_2 and ZnO are shown as1.2 eV and 3.4 eV, respectively.

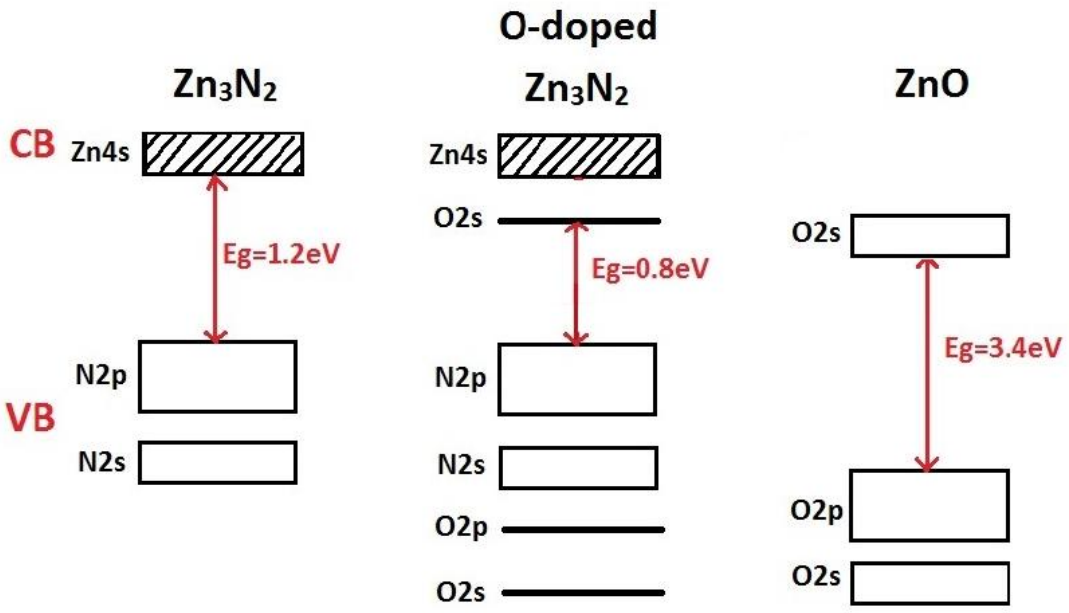

Figure 5-1. Schematic energy diagram for the oxygen doped Zn_3N_2 which shows the conduction band interacts with narrow energy band formed by adding small amount of oxygen

Powder XRD data demonstrates that there is a mix of Zn_3N_2 and ZnO powder. We speculate that the layer of ZnO forms around the Zn_3N_2 particles after exposure to air while the centre of the particles still contains Zn_3N_2. The ZnO layer will grow as a result of more oxidation of the Zn_3N_2 powders. But according to the different obtained bandgap from PL measurement, we conclude that there is a small amount of oxygen diffused into center of the Zn_3N_2 particles. Furthermore, after thermal nitriding of the O-doped Zn_3N_2 powder, our result shows the PL peak position shifts to higher energy around 1.2 eV. This means that nitriding the O-doped Zn_3N_2 powder increases the bandgap energy due to the removal of dispersed oxygen atoms from the center of the Zn_3N_2 particles. But the layer of ZnO still remains around Zn_3N_2 particles after nitriding. So at the end of nitriding, there is almost pure Zn_3N_2 in the center of particles with bandgap value of 1.2 eV. Figure 5.2 shows a schematic of the Zn_3N_2 particles after oxidizing and nitriding. This implies that the different electronic bandgap structure for Zn_3N_2 can be achieved by changing the oxygen content in the material through oxidizing or nitriding.

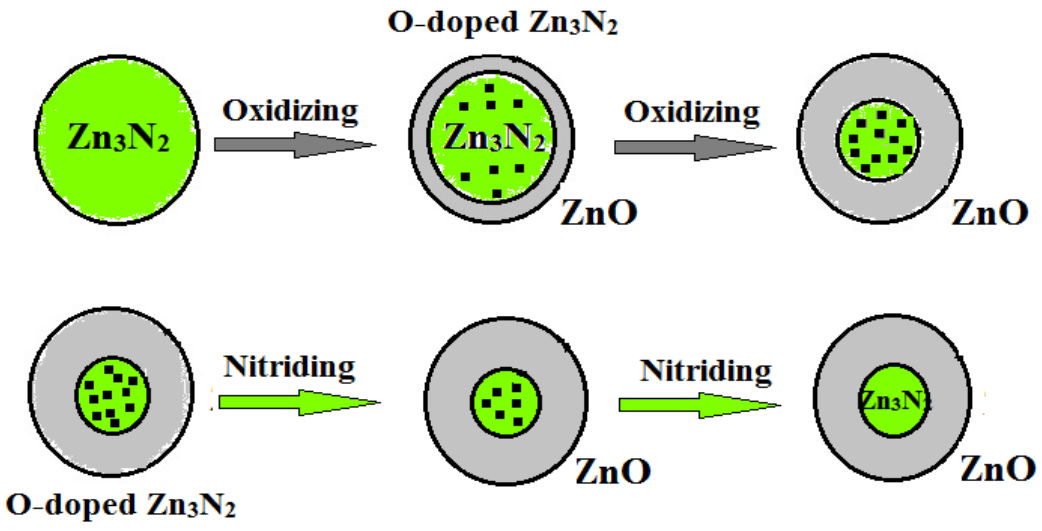

5-2. Schematic of Zn_3N_2 particles after oxidizing and nitriding

Conclusion

In this work, the optical bandgap energy of Zn_3N_2 powder has been obtained by two different techniques. The bandgap energy of zinc nitride powder was investigated using PL and DR measurements. Some samples of Zn_3N_2 powder with different oxygen contamination were used to study the effect of oxidation on the zinc nitride bandgap energy. Also, SEM and powder XRD have been used as structural characterization techniques.

SEM images showed the surface morphology of zinc nitride powders which had faceted shapes with micron size diameter. Powder XRD scans provided information as the crystal purity of ZnN powders. The oxygen contamination was determined for different powder samples under different annealing conditions by PXRD.

From the photoluminescence spectra of the samples, the bandgap energy and also the temperature dependence of the band gap energy has been studied. Room temperature PL measurements yield a bandgap of 1.12 eV for Zn_3N_2 powders. Due to the oxidation process, the PL spectra showed a peak shifting from at 1.12 eV to 0.85 eV which can be explained by anti-crossing interaction between the extended states of the conduction band of Zn_3N_2 and the localized oxygen states near the bottom of the conduction band. The low temperature PL showed that the bandgap energy is around 1 eV. Also a blue shift of photoluminescence peak was observed with decreasing the temperature.

To determine the bandgap energy of Zn_3N_2, the diffuse reflectance has been used as another technique. By using Kabulka-Munk formula, the relation between diffuse reflectance and optical absorption was found. The calculated bandgap from reflectance measurement verifies that Zn_3N_2 powder has a bandgap value of 1.12 eV. Also, similar to the PL result for different ZnN powders,

this bandgap value decreases in the presence of small concentrations of oxygen. The DR results have been compared to similar measurements made with a commercial UV-VIS spectrometer.

To study the effect of oxygen contamination on the ZnN bandgap energy, a thermal nitriding method was implemented. PL and PXRD results showed that the thermal nitriding process can cause an enhancement of the bandgap energy for O-doped Zn_3N_2 powder due to a reduction in oxygen content.

In addition, for analyzing micro-structural properties, the thermal oxidation was applied to fresh zinc nitride powder. The PXRD data of Zn_3N_2 powder as a function of thermal oxidation at different temperatures illustrates that bulk oxidation occurs rapidly at 500^oC and higher. This result confirms that Zn_3N_2 powder does not oxidize quickly at room temperature.

From our result, the optical bandgap is estimated to be ~1.2 eV for pure Zn_3N_2 powders which decreases with increasing oxygen. The oxygen as a more electro-negative anion creates bound states within the bandgap of Zn_3N_2. It can be concluded that the O/N ratio explains why the optical properties and band structure of Zn_3N_2 powder is a controversial subject for researchers. Clearly, controlling the oxygen-nitrogen ratio within the Zn_3N_2 structure is a key parameter for the optical properties and applications which needs further investigation. It is expected that this material will have some applications in photonics and solar cells in the future due to its appropriate bandgap energy, low materials cost and lack of toxicity.

References

1. V Kambilafka, P Voulgaropoulou, S Dounis, E Iliopoulos, M Androulidaki. The effect of nitrogen on the properties of zinc nitride thin films and their conversion into p-ZnO:N films. *Thin Solid Films*. 515, 8573 (2007).

2. R Kumar, O Al-Dossary, G Kumar, A Umar. Zinc Oxide Nanostructures for NO2 Gas–Sensor Applications:A Review. Nano-Micro Lett., 7, 97 (2015).

3. G Paniconi, Z Stoeva, R Smith, P Dippo, B Gallagher, and D Gregory. Synthesis, Stoichiometry and Thermal Stability of Zn_3N_2 Powders Prepared by Ammonolysis Reactions. *J. Solid State Chem.* 181, 158 (2008).

4. K Kurimaya, Y Takashi, F Sunohara. Optical band gap of Zn_3N_2 films. *Phys. Rev. B,* 48, 2781 (1993).

5. R Juza, H Hahn, Z Annorg. Allg. Chem., 244, 125 (1940).

6. D E Partin, D J Williams and M O'Keeffe. The Crystal Structures of Mg_3N_2 and Zn_3N_2. *J. Solid State Chem*. 132, 56 (1997).

7. M Futsuhara, K Yoshioka and O Takai. Structural, electrical and optical properties of zinc nitride thin films prepared by reactive rf magnetron sputtering. *Thin Solid Films*, 322, 274 (1998).

8. Z Li, P Wang, H H Chen, and X L Cheng. Structural, electronic and thermodynamic properties of cubic Zn_3N_2 under high pressure from first-principles calculations. *Physica B Condens Matter*. 406, 1182 (2011).

9. S Yoo, A Walsh, D Scanlon, A Soon. Electronic structure and band alignment of zinc nitride, Zn_3N_2. *RSC Adv.,* 4, 3306 (2014).

10. W S Khan, T Cao, C Cao, D Yu Ping, G Nabi, S Hussain, and F K Butt. Optical properties and characterization of zinc nitride nanoneedles prepared from ball-milled Zn powders. *Mater. Lett. ,* 65, 1264 (2011).

11. W S Khan, C Cao. Synthesis, growth mechanism and optical characterization of zinc nitride hollow structures. *J. Cryst. Growth*, 312, 1838 (2010).

12. P Taylor, M Schreuder, T Smeeton, A Grundy, J Dimmock, S Hooper, J Heffernan. Synthesis of widely tunable and highly luminescent zinc nitride nanocrystals. *J. Mater. Chem. c,* 2, 4379 (2014).

13. S R Bhattacharyya, R Ayouchi, M Pinnisch, R Schwarz. Transfer characteristic of zinc nitride based thin film transistors. *Physica Status Solidi. C, Current Topics in Solid State Physics*, 9, 469 (2012).

14. E Maile and R Fischer. MOCVD of the Cubic Zinc Nitride Phase, Zn_3N_2, Using Zn [N $(SiMe_3)_2]_2$ and Ammonia as Precursors. *Chem. Vap. Deposition*, 11, 409 (2005).

15. T Suda, & K Kakishita. Band-gap energy and electron effective mass of polycrystalline Zn_3N_2. *J. of App. Phys.* 99, 076101 (2006).

16. P Wu, T Tiedje, H Alimohammadi, V Bahrami-Yekta, M Masnadi-Shirazi, & C Wang. Molecular beam epitaxy growth and optical properties of single crystal Zn_3N_2 films. *Semicond. Sci. Technol.*, 31, 10 (2016).

17. D A Skoog, F J Holler, S R Crouch, *Principles of Instrumental Analysis*. Sixth Edition, Thomson Brooks/Cole, USA (2007)

18. P J Dean. Photoluminescence as a diagnostic of semiconductors. *Prog. Cryst. Growth & Charact.*, 5, 89 (1982).

19. D V Skobel′tsyn and Fizicheskiĭ institut imeni PN Lebedeva. Optical studies in liquids and solids. New York: Consultants Bureau (1969).

20. R Molenaar, J ten Bosch and J Zijp. Determination of Kubelka-Munk scattering and absorption coefficients by diffuse illumination. *Applied Optics*, 38, 2068 (1999).

21. P. Kubelka and F. Munk, Z. *Tech. Phys.* 12, 593 (1931).

22. A A Christy, O M Kvalheim, R A Velapoldi. Quantitative analysis in diffuse reflectance spectrometry: A modified Kubelka-Munk equation. *Vibrational Spectroscopy*, 9, 19 (1996).

23. P Kubelka. New Contributions to the Optics of Intensely Light-Scattering Materials. Part II: Nonhomogeneous Layers. *J. Opt. Soc. Am.* 44, 330 (1954).

24. J Torrent and V Barr´on, *Encyclopedia of Surface and Colloid Science.* (Marcel Dekker, Inc.) New York, (2002).

25. R A Smith, *Semiconductors*, 2nd ed. (Cambridge University Press: Cambridge (1978).

26. B Pejova, B Abay, and I Bineva. Temperature Dependence of the Band-Gap Energy and Sub-BandGap Absorption Tails in Strongly Quantized ZnSe Nanocrystals Deposited as Thin Films. *J. Phys. Chem. C*, 114, 15280 (2010).

27. P Lautenschlager, M Garriga, S Logothetidis and M Cardona. Interband critical points of GaAs and their temperature dependence. *Phys. Rev. B*, 35, 9174 (1987).

28. B Philips-Invernizzi, D Dupont and C Caze. Bibliographical review for reflectance of diffusing media. *Optical Engineering*, 40, 1082 (2001).

29. K Toyoura, H Tsujimura, T Goto, K Hachiya, R Hagiwara, Y Ito. Optical properties of zinc nitride formed by molten salt electrochemical process. *Thin Solid Films*, 492, 88 (2005).

30. T Yang, Z Zhang, Y Li, M Lv, S Song S, Z Wu. Structural and optical properties of zinc nitride films prepared by rf magnetron sputtering. *Appl. Surf. Sci.*, 255, 3544 (2009).

31. C Nunez, J Pau, M Hernandez, M Cervera, E Ruiz, J Piqueras. On the zinc nitride properties and the unintentional incorporation of oxygen. *Thin Solid Films*, 520, 1924 (2012).

32. H Kim , S Jeon, J Park, T Kim, K Son, J Seon, S Seo, S Kim, E Lee, J Chung, H Lee, S Han, M Ryu, S Lee. Anion control as a strategy to achieve high-mobility and high-stability oxide thin-film transistors. *Scientific Reports*, 3, 1459 (2013).

33. T Sakamoto, R Saki, T Moriga, K Murai, I Nakabayashi. Characterizations of zinc oxynitride powders prepared under ammonia gas flow. Int. J. Mod. Phys. B, 17, 1523 (2003).

34. Z Fu-Jian, M Hong-Lei, L Wei, D Wei, Z Xi-Jian, X Hong-Di, M Jin, J Feng, X Cheng-Shan, Z Hui-Zhao. Thermal Decomposition Behaviour of Zn_3N_2 Powder. *Chin. Phys. Lett.*, 22, 907 (2005).

35. T Wen, M Gautam, A Soleimanpour, A Jayatissa. Thermal annealing effect on zinc nitride thin films deposited by reactive rf-magnetron sputtering process. Mater. Sci. Semicond. Process., 16, 318 (2013).

36. R Long, Y Dai, L Yu, M Guo, and B B Huang. Structural, electronic, and optical properties of oxygen defects in Zn_3N_2. *J. of Phys. Chem. b*, 111, 3379 (2007).

37. N Akter, M Moshiur Rahman, & S Akter. Introducing a Phenomenon of Single Junction Multiple Band-gap Solar Cell Compared to Single Junction or Multi Junction Solar Cell to Achieve High Efficiency. ABC j. adv. res. [Online], 2.1, 30 (2016).

38. L Pauling. The Nature of the Chemical Bond and the Structure of Molecules and Crystals: An Introduction to Modern Structural Chemistry. (3d ed.) Ithaca, N.Y: Cornell University Press, (1960).

39. W Shan , W Walukiewicz, J Ager, K Yu, J Wu, E Haller, Y Nabetani, T Mukawa, Y Ito, T Matsumoto. Effect of oxygen on the electronic band structure in ZnOxSe1-x alloys. *Appl. Phys. Lett.* 83, 299 (2003).

40. N E Gorji. Oxygen incorporation into CdS/CdTe thin film solar cells. *Optical and Quantum Electronics*. 47, 2445 (2015).

41. R Singh, R Tay, W Chow, S Tsang, G Mallick, E Teo. Band gap effects of hexagonal boron nitride using oxygen plasma. *Appl. Phys. Lett.*104, 163101 (2014).

42. X Cao, A Sato, Y Ninomiya, and N Yamada. Oxygen-Doped Zinc Nitride as a High-Mobility Nitride-Based Semiconductor. *J. Phys. Chem c*, 119, 5327 (2015).

43. M Zervos, C Karipi and A Othonos. Zn_3N_2 nanowires: growth, properties and oxidation. *Nanoscale. Res. Lett.*, 8, 1 (2013).

44. CAMTEC workshop, Class notes "Scanning Electron Microscopy (SEM)" DR. Elaine Humphrey, University of Victoria, summer (2015).

45. J I Langford and A J C Wilson. Scherrer after Sixty Years: A Survey and Some New Results in the Determination of Crystallite Size. *J. Appl. Cryst.* 11, 102 (1978).

46. L Jingbo and Su-Huai Wei. Alignment of Isovalent Impurity Levels: Oxygen Impurity in II-VI Semiconductors. *Phys. Rev. B*, 73, 4 (2006).